Acta Pharmaceutica Sinica B 2026;16(8):5217−5236

Chinese Pharmaceutical Association
Institute of Materia Medica, Chinese Academy of Medical Sciences

Acta Pharmaceutica Sinica B

www.elsevier.com/locate/apsb
www.sciencedirect.com

ORIGINAL ARTICLE

Formic acid released by intratumoral *Bacteroides thetaiotaomicron* facilitates combinational therapy of Apatinib and aPD-1 in hepatocellular carcinoma

Jiongjiong Lu[a,†], Feiling Feng[b,†], Chunlei Li[c,†], Ziqing Yu[d,†], Tingting Zhang[e], Anchang Liu[c], Qingxiang Gao[b], Zhizhen Li[b], Li Luo[f,*], Xuemei Guan[g,*], Yanxiao Xiang[c,*], Hao Zhuang[e,*]

[a]*Department of Special Treatment, Eastern Hepatobiliary Surgery Hospital, Third Affiliated Hospital of Naval Medical University, Shanghai 200185, China*
[b]*Department of Biliary Tract Surgery I, Eastern Hepatobiliary Surgery Hospital, Third Affiliated Hospital of Naval Medical University, Shanghai 200185, China*
[c]*Department of Pharmacy, Qilu Hospital, Cheeloo College of Medicine, Shandong University, Jinan 250021, China*
[d]*Department of Geriatrics, The First Affiliated Hospital of Sun Yat-sen University, Guangzhou 510080, China*
[e]*Department of Hepatobiliopancreatic Surgery, The Affiliated Cancer Hospital of Zhengzhou University, Henan Cancer Hospital, Zhengzhou 450008, China*
[f]*Hospital Office of the President, GuiHang Guiyang Hospital, Guiyang 550009, China*
[g]*Medical Examination Center, Shanxi Province Cancer Hospital, Shanxi Hospital Affiliated to Cancer Hospital of Chinese Academy of Medical Sciences, Cancer Hospital Affiliated to Shanxi Medical University, Taiyuan 030013, China*

Received 21 June 2025; received in revised form 9 March 2026; accepted 13 March 2026

KEY WORDS

Hepatocellular carcinoma;
Immunotherapy;
Bacteroides thetaiotaomicron;

Abstract Through various murine models and 5 R−16 S sequencing, we identified *Bacteroides thetaiotaomicron* (*B.t*) as a sensitizer for the combined treatment of Apatinib and anti-PD-1 therapy. Clinically, *B.t* enrichment was associated with improved neoadjuvant treatment outcomes and a favorable prognosis in HCC patients. Mechanistically, *B.t* produces formic acid in tumor cells, inhibits aryl

*Corresponding authors.
E-mail addresses: 904211086@qq.com (Li Luo), guanxuemei_sx@163.com (Xuemei Guan), 11xiaoxiao23@163.com (Yanxiao Xiang), zhh8764@163.com (Hao Zhuang).
[†]These authors made equal contributions to this work.
Peer review under the responsibility of Chinese Pharmaceutical Association and Institute of Materia Medica, Chinese Academy of Medical Sciences.

https://doi.org/10.1016/j.apsb.2026.06.046

AhR;
Tyrosine kinase inhibitor;
Tumor metabolism;
Tumor microbiota;
Therapeutic response

hydrocarbon receptor (AhR) nuclear translocation by methylation, and suppresses downstream pathways, thereby mitigating pro-angiogenic effects and immunosuppression. The addition of formate or AhR inhibitors with combined treatment significantly enhanced therapeutic efficacy in preclinical models.

1. Introduction

Liver cancer, particularly hepatocellular carcinoma (HCC), poses a significant global health challenge as the third leading cause of cancer-related mortality[1]. For advanced stages of the disease, such as unresectable liver cancer, immune checkpoint inhibitors (ICIs) combined with anti-angiogenic agents have emerged as a first-line treatment[1]. Recent clinical trials have highlighted that the combinational regimen of ICIs with small-molecule anti-angiogenic drugs, such as Camrelizumab combined with Apatinib, offers longer overall survival (OS) compared to regimens with large-molecule anti-angiogenic agents (*e.g.*, ORIENT32, IMbrave150)[2,3]. Despite these advances, most patients receiving such combinations still experience disease progression or succumb to the disease within one to two years post-treatment, underscoring the urgent need to identify previously unknown factors influencing treatment sensitivity. Emerging research has identified a distinct liver microbiome that selectively originates from the gut[4]. Intratumoral bacteria have been detected in tumor tissues of HCC patients, with specific strains linked to tumor progression. For instance, *Stenotrophomonas maltophilia* has been shown to induce senescence in Hepatic stellate cells, thereby promoting HCC development[5]. These findings emphasize the clinical importance of understanding intratumoral bacteria in HCC. Notably, intratumoral bacteria can modulate treatment efficacy through various mechanisms. For example, *Fusobacterium nucleatum* has been found to activate the Toll-like receptor 4/myeloid differentiation primary response protein pathway and autophagy, leading to reduced chemotherapy efficacy in colorectal cancer[6]. Similarly, gut-derived *Lactobacillus reuteri* can colonize subcutaneous tumors and produce indole-3-aldehyde, which enhances the efficacy of immune checkpoint inhibitors in melanoma[7]. However, the role of intratumoral bacteria in influencing HCC treatment outcomes remains largely unexplored.

Short-chain fatty acids (SCFAs), including formic acid, acetic acid, propionic acid, and butyric acid, are key metabolic byproducts of bacterial activity[8]. Among these, formic acid plays a critical role in various cellular processes, such as pyrimidine and purine metabolism, as well as methylation cycles through one-carbon metabolism[9]. However, the role of formic acid in tumor biology remains controversial. On the one hand, endogenous formic acid, derived from tryptophan, can act as a one-carbon donor for purine synthesis, thereby promoting tumor proliferation[10]. On the other hand, formic acid or its endogenous precursor, serine, has been shown to enhance the proliferation and function of effector T cells[11,12]. This dual role highlights the complex interplay between bacterial-derived formic acid, tumor dynamics, and antitumor immunity. Understanding how formic acid coordinates these processes is essential for uncovering its regulatory potential in cancer treatment.

In this study, we identified a significant correlation between an increased burden of *Bacteroides thetaiotaomicron* (*B.t*) in hepatocellular carcinoma and improved efficacy of anti-angiogenic and ICIs therapies. Our *in vivo* and *in vitro* experiments revealed that *B.t* colonizes tumor cells and produces formic acid, which enhances one-carbon metabolism. This process inhibits aryl hydrocarbon receptor (AhR) nuclear translocation, thereby suppressing AhR-mediated pro-angiogenic effects through vascular endothelial growth factor A (VEGFA) and protein mono-ADP-ribosyltransferase TIPARP (TIPARP) pathways that otherwise contribute to tumor progression and immune suppression. Mechanistically, formic acid-mediated one-carbon metabolism was found to enhance methylation at AhR R13/R15 sites, directly inhibiting AhR nuclear translocation. Furthermore, our findings demonstrated that administering vancomycin in a somatic mouse model of HCC significantly increased intratumoral levels of *B.t*, leading to enhanced therapeutic efficacy of combination therapies and prolonged survival times.

2. Materials and methods

2.1. Patients and tissue samples

We analyzed two cohorts of patients with HCC from Shanghai Eastern Hepatobiliary Surgery Hospital and The Affiliated Cancer Hospital of Zhengzhou University between June 2020 and June 2023. HCC Cohort 1 consisted of 26 formalin-fixed, paraffin-embedded tissues, while HCC Cohort 2 included 36 fresh tissue samples. FISH studies were performed in HCC Cohort 1 to identify the presence and enrichment of *B.t* in response to treatment with Apatinib combined with anti-PD1 therapy. HCC Cohort 2 was used to examine the correlation between fatty acid metabolism and *B.t* load in HCC tumor tissues. All patients were pathologically and clinically diagnosed with HCC and subsequently received the stander combination therapy. Informed consent was obtained from all patients before sample collection, in accordance with institutional guidelines. Treatment efficacy was assessed through imaging systems and RECIST1.1. The study was approved by the Ethics Committee of Shanghai Eastern Hepatobiliary Surgery Hospital (Approval No. EHBHKY2021-K-038).

2.2. Animal experiments

C57BL/6 mice, C57BL/6JGpt-H11$^{em1Cin\ (Alb\text{-}CreERT2\text{-}polyA)}$/Gpt (Strain No. T017784) and C57BL/6JGpt-Ahr^{em1Cflox}/Gpt (Strain No. T008369) were obtained from Shanghai Eastern Hepatobiliary Surgery Hospital and The Affiliated Cancer Hospital of Zhengzhou University and maintained at the Animal Experiment Center. Germ-free mice were obtained from Shanghai Eastern Hepatobiliary Surgery Hospital and maintained at the Animal Experiment Center. All animal experiments were approved by the Animal Ethics Committee of Shanghai Eastern Hepatobiliary Surgery Hospital and the Affiliated Cancer Hospital of Zhengzhou University (Approval No. EHBHKY2021-K-038). For the HCC somatic mouse model, the 8-week-old C57BL/6 mice were

hydrodynamically injected *via* the lateral tail vein with a PBS/plasmid mix containing 10 μg of luc-pT3-MYC, 10 μg of pX330-p53, and 5 μg of CMV-SB13 transposase at a final volume of 10% of the body weight of the mouse as previous descripted[13]. For the Hepa1-6 ortho-model, 5×10^5 cells were suspended in 25 μL PBS and mixed with matrix glue at a rate of 1:1 and inoculated into the subcapsular space of the mouse liver through a median incision as previous descripted[14]. For the bacterial clearance, a mixture of 1 g/L Ampicillin trihydrate, 5 g/L Streptomycin sulphate, 1 g/Colistin sulfate and 0.25 g/L Vancomycin as previous descripted[15]. *In vivo* experiment: anti-PD-1 antibodies (200 μg per mouse, Bio × Cell, BE0146); anti-CD8α neutralizing antibodies (200 μg per mouse, Bio × Cell, BE0061); Apatinib (100 mg/kg, Selleck, S5248); Ch223191 (100 μg per mouse, MCE, HY-12684). For *sB.t* gavage, SPF mice, including $Ahr^{flox/flox}Alb^{CreERT2}$ heterozygous mice were gavaged with sterile PBS, *sB.t* WT strain or *sB.t* Δ*pflB* strain at a dose of 10^9 CFUs/200 mL in sterile PBS, respectively, once a day, and stopped at two days before treatment. For germ-free mice, sterile PBS or a dose of 3×10^9 CFUs/200 mL sB.t WT strain was only given once three days before further treatment. For tamoxifen induce *Ahr* ablation, $Ahr^{fl/fl}Alb^{CreERT2}$ mice were injected intraperitoneally with 75 μg/kg tamoxifen (MCE, HY-13757 A) for five consecutive days, followed by five recovery days to allow tamoxifen clearance before combining treatment.

2.3. Sample preparation, derivatization and gas chromatography-mass spectrometry (GC−MS)

Analysis was performed with slight modifications to the previously described procedure[16]. Prior to untargeted semi-quantitative GC−MS analysis, sample derivatization was carried out in two steps: ketone stabilization using methoxamine hydrochloride and *tert*-butyldimethylsilyl group derivatization. Following derivatization, GC−MS analysis was conducted on a GC system for the detection of highly volatile SCFAs; derivatization was performed in the organic phase using diethyl ether. A dilution series of a volatile free acid mix was prepared for quantification. Each reaction tube received 10 μL of 200 mmol/L ethylbutyric acid (internal standard), 1 mL of 99% diethyl ether, and 10 μL of 1 mmol/L hydrochloric acid. The tubes, primed with 190 μL of sample (fresh medium or ultrapure water as blanks), were agitated for 10 min at room temperature and then centrifuged at maximum speed for 5 min at 15 °C. The upper phase was transferred to a new 2-mL reaction tube. A second agitation-centrifugation-transfer cycle was performed by adding 1 mL of diethyl ether to the lower phase. Next, 250 μL of each sample was distributed into GC vials in triplicate, and 25 μL of MTBSTFA (with 1% *tert*-butyldimethylsilyl chloride) was added to each. The samples were then analyzed using GC−MS. Quantification of metabolite levels in mouse tumor interstitial fluid was performed using liquid chromatography-mass spectrometry (LC−MS) as described earlier (minimum volume: 50 μL; samples with yields below 50 μL were excluded).

2.4. Allelic exchange

BT4738 (encoding formate acetyltransferase/known as pyruvate formate-lyase, *pflB*) is a key enzyme responsible for formate production during intracellular fermentation in *B.t*. Deletion of the Δ*BT4738*(*pflB*) gene can be used to construct a formate metabolism-deficient strain[17]. The deletion mutants Δ*pflB* were generated using the pSIE1 plasmid system[18]. Briefly, nucleotide flanking regions around the deletion site were Gibson assembled into the linearized pSIE1 plasmid (SpeI and BamHI digested). The assembled plasmid was subsequently introduced into *B.t via* conjugation with *E. coli S17-1 λpir* and the conjugants were streaked onto BHISgent/erm plates. Resistant colonies were cultured overnight in TYG medium without antibiotics, and dilutions (10^{-1} to $^{-3}$) were plated onto BHIS agar with 100 ng/mL anhydrotetracycline (aTC). Colony PCR was used to confirm the intended deletions.

2.5. Strains, plasmids and media

B.t (BNCC354380) and the *B.t* Δ*pflB* strain were cultured and expanded following the procedure described previously[19]. All *B.t* strains were grown in TYG broth supplemented with 10% horse blood. The composition of one liter of TYG broth included 10 g of tryptone peptone, 5 g of yeast extract, 2 g of glucose, 100 mL of 1 mol/L KPO_4 (pH 7.2; prepared by mixing 1 L of 1 mol/L dibasic potassium phosphate in water with approximately 430 mL of 1 mol/L monobasic potassium phosphate in water to achieve pH 7.2), 40 mL of TYG salt solution (containing 0.5 g of $MgSO_4 \cdot 7H_2O$, 10 g of $NaHCO_3$, and 2 g of NaCl dissolved in 1 L of water), 1 mL of 0.8% $CaCl_2$ in water, 1 mL of 0.4 mg/mL $FeSO_4$ in water, 4 mL of 0.25 mg/mL resazurin in water, 1 mL of histidine hematin solution (1.2 μg/mL hematin, prepared by dissolving 12 mg of hematin in 10 mL of 0.2 mol/L histidine solution in water, pH adjusted to eight and filtered sterilized), 0.5 g of L-cysteine, and 1 mL of 1 mg/mL menadione in 100% ethanol. L-cysteine was resuspended in water (1 mL per 25 mg of L-cysteine) and filtered sterilized (0.22 μm filter) immediately prior to inoculation. The sterile histidine hematin solution, menadione, and L-cysteine were added to the autoclaved media just before inoculation. The media was pre-reduced by leaving it overnight inside an anaerobic chamber before inoculation, unless stated otherwise. Antibiotics were added when necessary: erythromycin (25 μg/mL), tetracycline (2 μg/mL), and gentamicin (200 μg/mL). Antibiotics for *B.t* were only used post-conjugation for selection and were not used during growth.

2.6. Anaerobic growth

All *B.t* strains were cultured statically in an incubator at 37 °C inside the anaerobic chamber. Oxygen within the anaerobic chamber was continuously removed by the Palladium Catalyst, which was replaced weekly by incubating it overnight (or longer) at 90 °C in the oven. Nitrogen was used to purge the air inside the airlock and to maintain a positive pressure within the anaerobic chamber. Oxygen and hydrogen levels within the chamber were monitored using an anaerobic monitor. The oxygen concentration inside the chamber was maintained at 0 parts per million, except when the inner door of the airlock was opened to transfer items in and out of the chamber. In such instances, low levels of oxygen were briefly introduced but were rapidly removed. Hydrogen concentration was kept above 1.5% to ensure proper functioning of the palladium catalyst, by adding a gas mix consisting of 5% H_2, 20% CO_2, and N_2. When moving items in and out of the chamber, the default P1 program was followed, which involved two cycles of vacuum and purge gas (N_2), followed by one cycle of vacuum and gas mix.

2.7. Co-culture of tumor cells and B.t

Adherent tumor cells were co-cultured with *B.t*. At 12 h after seeding, *B.t*. was counted and added to a specifically prepared

medium (DMEM with 10% fetal bovine serum, supplemented with 0.5 mL of histidine hematin solution, 0.25 g of L-cysteine, and 0.5 mL of 1 mg/mL menadione in 100% ethanol) at a multiplicity of infection (MOI) of 5:1. Tumor cells were initially cultured under anaerobic conditions. From that point onward, all procedures were performed under anaerobic conditions. After incubating for 12 h, the co-culture medium was removed, and the cells were washed with PBS.

2.8. ELISA for anti-PD1 antibody

Briefly, blood samples were collected in Heparinized-EDTA tubes and centrifuged at 4 °C for 2465×*g* (Eppendorf AG, 22,331, Hamburg, Germany) for 15 min to obtain the plasma, which was kept at −20 °C until use. The stock solution for ELISAs was prepared using this drug-free plasma diluted 1:150 (*v*/*v*) in incubation buffer (IB; 0.05% Tween-20, 0.1% BSA in DPBS), obtaining the matrix buffer (MB). This MB was spiked with different known drug concentrations to prepare the standard samples and the analytical control, which corresponded to free-drug MB. Calibration Standard Curves: two working solutions or stocks, 500 ng/mL for a-PD-1 and 250 ng/mL for a-PD-L1, were freshly prepared in MB to build the corresponding calibration standard curves. For ELISA procedure, 24 h before performing the assay, a flat-bottomed 96-well microplate was coated with 2 μg/mL of recombinant mouse-PD-1 capture fusion protein diluted in DPBS and incubated at 4 °C overnight. Afterward, the plate, washed twice with 200 μL/well of DPBS, was blocked with 200 μL/well of IB for 1 h at room temperature (RT) to prevent nonspecific reactions. Then, the plate was washed five times using 200 μL/well of washing buffer, and the standards and experimental samples were added and incubated for 2 h at RT. For the labeling, the plate was washed and treated for 1 h with a secondary goat a-rat IgG antibody. In order to amplify this signal, a goat IgG HRP-conjugated antibody was added and incubated for 1 h at RT.

The plate was washed and revealed with 100 μL/well of TMB for 3 min. This reaction was stopped by adding 50 μL/well of sulphuric acid, and the absorbance was read at 450 nm.

2.9. LC/MS−MS for Apatinib and vancomycin

Blood samples were collected in Heparinized-EDTA tubes and centrifuged at 4 °C for 2465×*g* (Eppendorf AG, 22,331, Hamburg, Germany) for 15 min to obtain the plasma, which was kept at −20 °C until use. For Apatinib detection[20], a sample aliquot of 10 μL was injected onto the column on a mass spectrometer equipped with an electrospray ionization source operating in the positive ion mode. For Vancomycin detection, plasma levels were measured after mixing 50 μL of serum and 100 μL of 10% trichloroacetic acid in a microtube, followed by vortex-mixing and centrifugation. A sample aliquot of 1 μL was injected onto the column on the UHPLC chromatography system operating in the positive ion mode.

2.10. Culturomics

B.t (BNCC354380) was isolated as previously described with modifications[7]. Tumor tissues were sterilely excised, divided into two parts, and homogenized in 0.05% NP-40 by grinding through a 40 μm filter in a 6-well plate. The tumor homogenate was incubated at 37 °C under anaerobic conditions for 3 h. The homogenate was then diluted 1:3 with sterile PBS, centrifuged at 2348×*g* (Eppendorf SE, Barkhausenweg 122,339, Hamburg, Germany) for 7 min to pellet the tumor tissue and bacteria, and the supernatant was discarded to remove any remaining lysis buffer. The pelleted tumor homogenate was resuspended in sterile PBS and transferred into TYG broth supplemented with 10% horse blood. The tumor culture broth was incubated anaerobically at 37 °C for 48 h in stationary conditions. Following incubation, the culture broth was streaked onto blood agar plates for single colony isolation. The agar plates were incubated anaerobically at 37 °C for 72 h. Single colonies were then selected from the agar plates for 16 S rRNA sequencing.

2.11. Fluorescence in situ hybridization (FISH)

Sequential tumor sections were subjected to fluorescence *in situ* hybridization (FISH) assays using the Enhanced Sensitive FISH Detection Kit IV (BOSTER). A Cy3-labeled total bacteria probe (EUB338-GCTGCCTCCCGTAGGAGT) and a *B.t*-specific probe (*B.t* specific-CATTTGCCTTGCGGCTA), targeting 16 S rRNA, were designed as previously reported[21].

2.12. Quantification of bacteria

Bacteria quantification was performed as described previously[22]. An equal amount of DNA (250 ng/μL) was used to amplify the V1−V2 region on the Light Cycler 480 Real Time PCR System (Roche) using specific primers. Total bacteria: F-AGAGTTTGATCMTGGCTCAG; R-TGCTGCCTCCCGTAGGAGT; *B.t*: F-GCAAACTGGAGATGGCGAC; R-AAGGTTTGGTGAGCCGTTA; *B.c*: F-GTCGGAATCCTGCTGAGAGGC; R-AACCCTCTGCTCCGACCATT; *H.a*: F-GGGATAACTAGTCGAAAGACT; R-ATATTAGCTACTACCGTTTCTTCC; *M.m*: F1-AGGTTGATTAGTGGCGAACGGG; R-CTTCGGACCTTGCGTTAATGGA; *C.l*: F-GTTCGGAATAACTCGCCGA; R-TCTTACGCGGGCTCATCCC. DNA extraction controls and paraffin controls were included for each cohort. *E. coli* genomic DNA was used to generate a standard curve for quantifying the absolute bacterial load.

2.13. Live in situ bacteria labeling with fluorescent D-alanine

Tumor cells were seeded and co-cultured as described earlier. After a 12-h incubation, the co-culture medium was removed, and the cells were washed with PBS. Tumor cells were then incubated in specifically prepared medium containing either FITC-labeled D-alanine (Sigma−Aldrich, SBR00049-5 MG) or DMSO control for 2 h under anaerobic conditions. Following this, tumor cells were fixed in 4% PFA for 4 h at room temperature and stained with DAPI. D-Ala-positive tumor cells were counted using the Vectra Polaris imaging system.

2.14. 16 S amplification and deep sequencing and analysis

16 S rRNA gene amplification, reconstruction, and analysis were performed as previously described[23,24]. Briefly, five regions of the 16 S rRNA gene were amplified using 100 ng DNA as input with a set of 10 multiplexed primers (F1: 5′-TGGCGAACGGGTGAGTAA-3′; F2: 5′-ACTCCTACGGGAGGCAGC-3′; F3: 5′-GTGTAGCGGTGRAATGCG-3′; F4: 5′-GGAGCATGTGGWTTAATTCGA-3′; F5: 5′-GGAGGAAGGTGGGGATGAC-3′; R1: 5′-AGACGTGTGCTCTTCCGATCTCCGTGTCTCAGTCCCARTG-3′; R2: 5′-AGACGTGTGCTCTTCCGATCTGTATTACCGCGGCTGCTG-3′; R3: 5′-AGACGTGTGCTCTTCCGATCTCCCGTCAATTCMTTTGAGTT-3′; R4: 5′-AGACGTGTGCTCTTCCGATCTCG

TTGCGGGACTTAACCC-3′; R5: 5′-AGACGTGTGCTCTTCC-GATCTAAGGCCCGGGAACGTATT-3′), 0.2 mmol/L dNTPs (Larova GmbH), and 0.02 U/μL Phusion Hot Start II DNA Polymerase (Thermo Scientific) for the first PCR reaction. Barcodes and Illumina adaptors were added to the amplicons in a second PCR reaction with 5 forward primers (FF1: 5′AATGATACGGCGAC CACCGAGATCTACACTCTTTCCCTACACGACGCTCTTCCG ATCTTGGCGAACGGGTGAGTAA-3′; FF2: 5′AATGATACGG CGACCACCGAGATCTACACTCTTTCCCTACACGACGCTCT TCCGATCTACTCCTACGGGAGGCAGC-3′; FF3: 5′AATGATA CGGCGACCACCGAGATCTACACTCTTTCCCTACACGACGC TCTTCCGATCTGTGTAGCGGTGRAATGCG-3′; FF4: 5′AATG ATACGGCGACCACCGAGATCTACACTCTTTCCCTACACGA CGCTCTTCCGATCTGGAGCATGTGGWTTAATTCGA-3′; FF5: 5′AATGATACGGCGACCACCGAGATCTACACTCTTTCC CTACACGACGCTCTTCCGATCTGGAGGAAGGTGGGGATG AC-3′) and one 8-nucleotide barcode-specific reverse primer (RR5: 5′CAAGCAGAAGACGGCATACGAGATNNNNNNNNGTGAC-TGGAGTTCAGACGTGTGCTCTTCCGATCT-3′). PCR products were purified using AMPure XP beads (Beckman Coulter Genomics, Danvers, MA, USA) and quantified using a Qubit fluorometer (Invitrogen, USA). The purified PCR products were evaluated using an Agilent 2100 Bioanalyzer (Agilent, USA) and a library quantification kit from Illumina (Kapa Biosciences, Woburn, MA, USA). Qualified library concentrations were above 0.3 ng/μL. The sequencing libraries (with non-repetitive index sequences) were diluted and mixed as required, then denatured with NaOH to generate single strands for sequencing. Double-end sequencing was performed on the Illumina NovaSeq 6000 sequencing platform using PE150 sequencing mode with the NovaSeq 6000 SP Reagent Kit (500 cycles). After data fractionation and filtering, Short Multiple Regions Framework (SMURF) analysis was performed for reconstruction. The sequences of the five amplified regions were integrated and analyzed for taxonomic identification of the bacteria. Contaminating bacteria introduced during sample collection, DNA extraction, and PCR amplification were removed. Subsequent microbiome analysis was based on the filtered flora data. Alpha diversity and beta diversity analyses were performed based on the resulting species-level abundance tables. The abundance of each species in each sample was quantified based on the species abundance tables. Differences between comparison groups were analyzed based on the species abundance statistics. Functional information was predicted using PICRUSt2 software, and variance analysis was performed with STAMP (Statistical Analysis of Metagenomic Profiles).

2.15. SAM and SAH detection

SAM and SAH levels were semiquantified as previously described[25]. At least 5×10^6 tumor cells were analyzed. Tumor cells were precipitated by methanol under vigorous shaking for 2 min, followed by centrifugation. The resulting extract was then split into two fractions for analysis using two separate reverse phase/UPLC−MS/MS methods, both employing positive ion mode electrospray ionization. L-Leucine-d_3 was used as the quality control standard. The analysis utilized a UPLC system coupled with a high-resolution/accurate mass spectrometer. The mass spectrometer was interfaced with a heated electrospray ionization source and an Orbitrap mass analyzer operated at 35,000 mass resolution. SAM and SAH were specifically analyzed under acidic positive ion conditions optimized for hydrophilic compounds. In this method, the extract was gradient-eluted from a C18 column (Waters UPLC BEH C18-2.1 mm × 100 mm, 1.7 μm) using a mobile phase composed of water and methanol, both containing 0.05% perfluoropentanoic acid and 0.1% formic acid. MS analysis alternated between MS and data-dependent MSn scans, with dynamic exclusion employed. Raw data were extracted, peaks identified, and QC processed using Metabolon's proprietary hardware and software. Peak intensities were quantified using the area-under-the-curve method, and data were normalized by dividing the peak areas by the median of the samples for relative quantification.

2.16. Cell culture

Hepa1-6, HUH7, and MHCC97-H were cultured in DMEM with 10% FBS. H22 were cultured in RPMI-1640 with 10% FBS.

2.17. The concentrations of drugs and reagents

In vitro experiment: SF (1 mmol/L); SB (1 mmol/L); EN4 (2 μmol/L); C188-9 (5 mmol/L); YC1 (2 μmol/L); Ch223191 (2 μmol/L); BAY-218 (5 mmol/L); KYN (50 mmol/L); KYNA (40 μmol/L); LMB (10 nmol/L); Importazole (5 μmol/L); AGI-24512 (1 μmol/L); AdOx (1 mmol/L); Apatinib (5 μmol/L).

2.18. Immunofluorescence

For immunofluorescence, tissue paraffin sections were cut to a thickness of 3 μm. After antigen retrieval and permeabilization, the sections were incubated with a diluted primary antibody against CD31, following the manufacturer's instructions, using the PANO 7-plex reagent kit (PANOVUE, 10,217,100,100). After antibody incubation, the sections were counterstained with DAPI to visualize the nuclei.

2.19. Flow cytometry

The liver orthotopic tumors or subcutaneous tumors carrying Hepa1-6 tumor cells were harvested and digested into single-cell suspensions. For cell surface marker analysis, all samples were stained with a live/dead dye at room temperature for 15 min, followed by incubation with various antibodies. The cells were then resuspended in PBS containing 1% FBS and incubated with the specified fluorescent-conjugated antibodies at 4 °C for 30 min. For intracellular staining and permeabilization, a fixation and permeabilization buffer (Invitrogen) was used according to the manufacturer's instructions. To assess cell death proportions, cells were dissociated using 0.25% trypsin (without EDTA), followed by centrifugation to collect the cells. The cells were then stained and analyzed using an apoptosis kit (BioLegend), according to the manufacturer's instructions.

2.20. Cell proliferation assays

Cell Counting Kit-8 was used to assess cell proliferation. Cells were seeded into a 96-well plate at a density of 2000 cells per well. Following the manufacturer's instructions, cell viability was measured at 0-, 24-, 48-, and 72-h post-seeding using the CCK-8 system.

2.21. Western blot and Co-IP

After transfection or stimulation, whole cell extracts were prepared and incubated with magnetic beads. The beads were washed

five times with low-salt lysis buffer, and the immunoprecipitates were then eluted. The samples were separated by SDS-PAGE and transferred to NC membranes. Primary antibodies targeting the protein of interest were applied according to the manufacturer's instructions. Horseradish peroxidase-conjugated secondary antibodies (CST) were used, and antigen−antibody complexes were detected by enhanced chemiluminescence.

2.22. Cytoplasmic and nuclear fractionation

Cytoplasmic and nuclear protein fractions were extracted using the NE-PER Nuclear and Cytoplasmic Extraction Reagents (Thermo Fisher Scientific) according to the manufacturer's protocol. The extracted proteins were then separated by SDS-PAGE for subsequent detection.

2.23. qRT-PCR

RNA was extracted from the indicated cells, and first-strand cDNA was synthesized using a reverse transcription kit (Promega). RT-qPCR was performed on a LightCycler® 480 Instrument II System (ROCHE, Switzerland). The data were normalized to GAPDH expression for analysis. Supporting Information Table S1.

2.24. ELISA assay

Supernatants were collected for subsequent ELISA assays. Mouse tumor tissue samples were weighed and extracted using Tissue Protein Extraction Reagent (Thermo Fisher Scientific). All experiments were conducted following the manufacturer's instructions. Supporting Information Table S2.

2.25. Gene edition

The sgRNA target sequence was cloned into the PX458 plasmid. Cells were transfected and flow-sorted, then diluted to single cells and seeded into 96-well plates. After cell expansion, gene knockout efficiency was verified by Western blot. Short interfering RNAs (siRNAs) targeting the indicated genes were designed and synthesized by GenePharma (Shanghai, China). Transfection was carried out using RNAiMAX (Invitrogen) following the manufacturer's protocol, and knockdown efficiency was assessed by qPCR (Table S1).

2.26. ChIP assay

Chromatin immunoprecipitation (ChIP) assays were performed using the Pierce Magnetic ChIP Kit (Thermo Fisher Scientific). Briefly, cells were cross-linked with 1% formaldehyde and quenched with glycine. Fixed cells were harvested, lysed, and subjected to multiple rounds of sonication on ice, with 30-s incubations between pulses. Immunoprecipitation was carried out using specific antibodies, and the precipitated DNA was subsequently amplified by qPCR (Table S1).

2.27. Luciferase assay

Cells were seeded into 12-well plates and incubated for 12 h, followed by co-transfection with the empty vector or vector encoding AhR, along with the reporter plasmid and phRL-TK-*Renilla* luciferase control vector (Addgene). After 24 h, cells were lysed by adding the specified reagents as per the manufacturer's instructions. Luciferase activity was then measured using a dual-luciferase analyzer (Promega). Firefly luciferase activity was normalized to *Renilla* luciferase activity for each sample (Supporting Information Table S3).

2.28. Statistical analysis and reproducibility

Data are expressed as mean ± standard error of mean (SEM) or mean ± standard deviation (SD) of at least three independent experiments. Statistical analyses were performed using GraphPad Prism 10 or SPSS Statistics. Two-tailed Student's *t*-test, two-tailed Wilcoxon tests, and one-way ANOVA with Tukey's *post hoc* tests were used to calculate *P* values. Time-to-event data were described using Kaplan−Meyer curves. *P* values less than 0.05 were considered statistically significant. All experiments were performed in triplicate unless otherwise indicated.

3. Results

3.1. B.t enrichment promotes efficacy of aPD1+TKI treatment in hepatocellular carcinoma

The presence of bacteria has been reported in both normal liver tissue and hepatocellular carcinoma (HCC)[26,27]; however, its impact on HCC treatment remains unclear. Given that the bacteria in the liver are predominantly derived from intestinal microbiota, and considering that over 40% of the gut flora genus in mice overlap with those in humans[28,29], we constructed a somatic HCC mouse model (Supporting Information Fig. S1A). We first confirmed the presence of bacteria in both healthy liver and tumoral tissues (Fig. S1B). To investigate whether intratumoral bacteria influence the effectiveness of neoadjuvant therapy (aPD-1 + TKI) for HCC, we employed two antibiotic regimens including antibiotic cocktail (ABX, a mixture of Ampicillin Trihydrate, Streptomycin sulphate, Colistin sulfate, and Vancomycin) that targeting both Gram-positive (G+) and Gram-negative (G−) bacteria and vancomycin which selectively targeting G+ bacteria (Fig. 1A). Interestingly, we observed that vancomycin significantly enhanced the efficacy of the aPD-1 and Apatinib combination therapy, resulting in an increased tumor inhibition rate and prolonged survival. In contrast, ABX treatment led to a marked decrease in therapeutic efficacy (Fig. 1B−D). By monitoring the changes in plasma drug concentration of aPD-1 antibody or Apatinib, we found that whether the mice received vancomycin or not did not affect pharmacokinetics of these two drugs (Fig. S1C). We also monitored the changes in vancomycin concentration in the livers of mice and found that even when treating multiple murine (Hepa1-6, H22) or human (MHCC97-H, HUH7) hepatocellular carcinoma cell lines with the highest (∼0.5 ng/g) concentration detected, it did not affect the growth of any of the cell lines (Fig. S1D and S1E). These findings suggest that the G− bacteria contribute to the enhanced efficacy of aPD-1 + TKI therapy in HCC. Notably, in the absence of aPD-1 + TKI therapy, neither antibiotic regimen had a significant effect on tumor growth either (Fig. 1B and C).

We then sought to determine whether the sensitizing effect of vancomycin on aPD-1 + TKI therapy in HCC could be attributed to a specific species or strain of bacteria. To address this, we assessed the bacterial composition of mouse HCC tumor masses using 5 R−16 S sequencing. Comparative analysis of different experimental groups: group 1 (mG1; vancomycin *vs.* PBS; 6 *vs.*

6); group 2 (mG2; PBS *vs.* ABX; 6 *vs.* 6). After quality control (Fig. 1E and Fig. S1F−S1H), we revealed that several G− bacteria, including *B.t*, *Methylotenera mobilis* (*M.m*), *Burkholderia cepacia* (*B.c*), *Caulobacter leidyi* (*C.l*), and *Herbaspirillum aquaticum* (*H.a*), met the following criteria: 1) they were enriched in the HCC tumors from mice treated with vancomycin; 2) their levels were higher in mice treated with PBS compared to those treated with ABX (Fig. 1F and Fig. S1I). Subsequently, we established an HCC cohort-1 ($n = 26$, responders = 16, non-responders = 10) and assessed the levels of these five candidate bacterial species in the cohort samples using qPCR with species-specific primers after establishment of a standard curve (Fig. S1J). Interestingly, we found that only *B.t* was significantly enriched in the responders, while the other bacteria were either barely detected or exhibited no significant enrichment (Fig. S1K−S1M). Finally, to confirm the presence of *B.t* in the tumor tissues, we performed fluorescence *in situ* hybridization (FISH) using *B.t*-specific probes on tumor slides from HCC Cohort-1. Our results confirmed that *B.t* was present in the tumor tissues, and its enrichment was notably higher in responders compared to non-responders (Fig. 1G).

To further investigate the biological effect of *B.t*, we acquired the standard BNCC 354380 strain (*sB.t*). Previous studies have shown that *Bacteroides* can invade and survive within host cells[30]. To explore the interaction between *sB.t* and liver tumor cells, firstly, we tested several Multiplicity of Infection (MOI = 0/1/5/10); and found that after 12 h of co-culture, both human Hepatic cancer cell line MHCC97-H and the murine Hepatic cancer cell line Hepa1-6 exhibited significant death and further growth inhibition when the MOI was 10, whereas there were no significant changes in cell status when the value was 5 (Fig. S1N and S1O). More strikingly, electron microscopy revealed that *sB.t* predominantly colonized the cytoplasm of the tumor cells (Supporting Information Fig. S2A). To confirm that the colonized bacteria were alive and metabolically active, we incorporated fluorescently labeled D-alanine into the co-culture system and successfully detected intracellular labeling. Notably, under MOI = 5, more than 80% of cells from both the MHCC97-H and Hepa1-6 cell lines exhibited *sB.t* colonization (Fig. S2B). Next, we extended this investigation to an *in vivo* model by performing intraHepatic injection of Hepa1-6 cells colonized with *sB.t* into C57BL/6 mice (Fig. 1H). Seven days post-injection, tumor masses were excised. Quantitative PCR (qPCR) analysis confirmed that *sB.t* accounted for more than 40% of the total bacteria present within the tumors (Fig. S2C and S2D). When homogenates from the excised tumor mass were plated on culture plates, bacterial clones were observed, and qPCR analysis confirmed that these colonies were viable *sB.t* (Fig. S2E). Moreover, after inoculating Hepa1-6 cells carrying s*B.t* into the livers of germ-free (GF) mice, we found that systemic administration of the ABX regimen could also significantly reduce the amount of s*B.t* in tumors formed by Hepa1-6 cells (Fig. S2F). Then the impact of *sB.t* on the efficacy of aPD-1 + Apatinib therapy was further tested in the Hepa1-6-based orthotopic liver cancer model and we found that aPD-1 + TKI treatment resulted in smaller tumor volumes and prolonged survival in mice injected with *sB.t*-colonized tumor cells, compared to those without *sB.t* (Fig. 1I and Fig. S2G). More importantly, to better clarify the effect of *B.t* under *in vivo* conditions, we utilized GF mice and established a somatic HCC model, while administering s*B.t* by gavage. After confirming the presence of *B.t* in the formed primary liver tumors (Fig. 1J), we conducted treatment with aPD-1 antibody combined with Apatinib and found that in the presence of *B.t*, the combined treatment resulted in smaller tumor volumes (Fig. 1K). Interestingly, we also noticed that under the treatment of Apatinib, the content of s*B.t* in liver tumors was higher, while no significant changes in the colonization of s*B.t* under aPD-1 antibody treatment were observed (Fig. 1L). Together, the above data indicated that *B.t* played an important role in bacteria-mediated aPD-1 antibody/Apatinib combination therapy enhancement.

3.2. B.t promotes the efficacy of Apatinib and aPD-1 by respectively inhibiting VEGFA and promoting IFN-is transcription

Next, we aimed to elucidate the mechanism by which *B.t* enhances the efficacy of aPD-1 + TKI therapy. In our initial investigations, we tested the effects of *sB.t* on aPD-1 or Apatinib alone. Interestingly, *sB.t* universally enhanced the efficacy of both aPD-1 and Apatinib as standalone therapies (Fig. 2A). To explore the specific interaction between *B.t* and Apatinib, we first evaluated whether *sB.t* affected Apatinib-induced cell death. Co-culture experiments with Hepa1-6 cells showed no significant differences in cell death after Apatinib treatment compared to cells without *sB.t* (Supporting Information Fig. S3A). Similar results were observed with the MHCC97 cell line (Fig. S3B). Given that Apatinib suppresses tumor growth primarily through anti-angiogenesis[31,32], we next examined its effect on tumor vascularization. *In vivo*, we found that tumors formed by *sB.t*-colonized Hepa1-6 cells did not exhibit significant differences in vascular density compared to tumors without *sB.t* in the absence of Apatinib. However, after Apatinib treatment, the vascular density in tumors containing *sB.t* was significantly lower (Fig. 2B). These findings suggest that *sB.t* enhances Apatinib efficacy by potentiating its anti-angiogenic effects. Since vascular endothelial growth factor receptor 2 (VEGFR2), the primary target of Apatinib, is activated by VEGFA, vascular endothelial growth factor C (VEGFC), and vascular endothelial growth factor D (VEGFD)[33], we assessed the expression of these genes by qPCR in *sB.t*-co-cultured Hepa1-6 and MHCC97 cells. While *sB.t* co-culture weakly downregulated *VEGFA*, the expression levels of *VEGFC* and *VEGFD* remained unchanged (Fig. S3C and S3D). Notably, under Apatinib treatment, *sB.t*-colonized cells showed significant downregulation of *VEGFA*, whereas Apatinib alone induced baseline upregulation of *VEGFA* (Fig. 2C and Fig. S3E). These data indicate that *sB.t* enhances Apatinib efficacy by suppressing VEGFA production, thereby further inhibiting angiogenesis and promoting tumor suppression. To confirm this, we generated *Vegfa*-knockout Hepa1-6 cells (Fig. S3F). In these cells, the differences in tumor volumes between *sB.t*-colonized and non-colonized tumors were almost completely abolished under Apatinib treatment. Both groups exhibited similarly low levels of intratumoral blood vessels (Fig. 2D). Together, these findings demonstrate that *sB.t* enhances the anti-angiogenic efficacy of Apatinib by downregulating VEGFA, contributing to improved tumor suppression.

We next investigated the mechanisms by which *B.t* enhances the efficacy of aPD-1 therapy. Considering that the number and functional status of $CD8^+$ T cells within tumors are critical for the effectiveness of aPD-1[34], we analyzed $CD8^+$ T cell infiltration and the expression of key effector molecules, IFNγ and TNFα. We observed increased $CD8^+$ T cell infiltration in tumors formed by *sB.t*-carrying Hepa1-6 cells; however, the expression levels of effector molecules were significantly lower compared to tumors without *sB.t*. Following aPD-1 treatment, although differences in $CD8^+$ T cell infiltration persisted between the two tumor types,

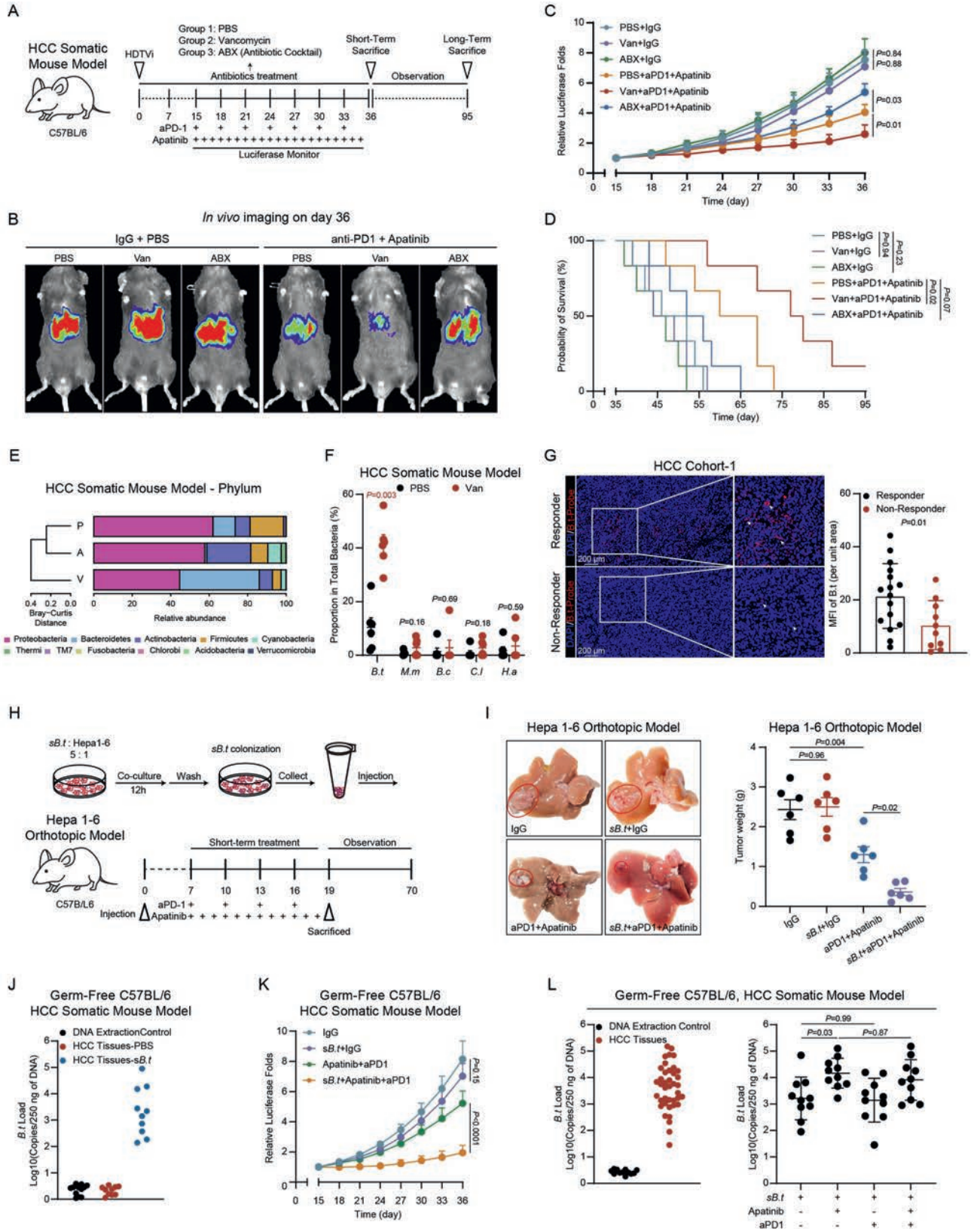

Figure 1 *B.t* enrichment promotes efficacy of aPD1+TKI treatment in hepatocellular carcinoma. (A) Schematic diagram of the treatment protocol for HCC somatic mouse model. (B, C) Representative image (B) and relative fold change (compared to Day 15) of luciferase intensity in the HCC somatic mouse model (C) ($n = 6$ per group), P value by one-way ANOVA, mean ± SD. (D) Survival curve of the HCC somatic mouse model after indicated treatment ($n = 6$ per group). (E) Taxonomic microbial composition detected in tumor samples. Relative abundance of bacterial communities in HCC somatic mouse model after indicated treatment ($n = 6$ per group) is displayed at phylum level. (F) Statistical

the functional status of $CD8^+$ T cells in *sB.t*-containing tumors, as indicated by IFNγ and TNFα expression, was restored to levels comparable to those in tumors without *sB.t* (Fig. 2E and Fig. S3G). This suggests that while *sB.t* promotes $CD8^+$ T cell infiltration, it concurrently induces functional exhaustion, which is reversed by aPD-1, resulting in synergistic effects. To confirm that the synergy between *sB.t* and aPD-1 depends on $CD8^+$ T cells, we used a CD8-depleting antibody. This ablation completely abolished the synergistic effect of *sB.t* with aPD-1, verifying the central role of $CD8^+$ T cells (Fig. S3H). Since $CD8^+$ T cell exhaustion is characterized by reduced effector molecule expression, we hypothesized that *sB.t* promotes $CD8^+$ T cell infiltration while simultaneously inducing exhaustion. Given that $CD8^+$ T cell infiltration and exhaustion are strongly influenced by cytokine profiles, we examined the inflammatory cytokines using ELISA screening in Hepa1-6 cells with and without *sB.t* cells. Carrying *sB.t* showed significant upregulation of type I interferons (IFNα and IFNβ) at protein levels, as confirmed by qPCR (Fig. 2F and Fig. S3I). Type I interferons (IFN-Is) are known to promote $CD8^+$ T cell infiltration while contributing to their exhaustion[35]. To clarify the involvement of IFN-Is, we generated an *Irf3*-knockout Hepa1-6 cell line (Fig. S3J), as IRF3 is a key regulator of IFN-Is production, activated by sensing damage-associated molecular patterns or pathogen-associated molecular patterns (PAMPs). In *Irf3*-knockout cells, the differences in IFNα and IFNβ expression between *sB.t*-carrying and control cells disappeared (Fig. 2G). Furthermore, the synergistic effect of *sB.t* and aPD-1 therapy was nearly eliminated, with no significant differences in $CD8^+$ T cell infiltration between groups (Fig. S3K). Moreover, in somatic HCC model established in GF mice, under Apatinib combined with aPD-1 antibody treatment, it was found that administering s*B.t* also led to an increase in the proportion of $CD8^+$ T cells among the infiltrated immune cells, accompanied by downregulated *Vegfa* expression as well as increased levels of *Ifna2/b1* (Fig. 2H and I). In summary, these findings demonstrate that *sB.t* enhances the efficacy of aPD-1 therapy by promoting $CD8^+$ T cell infiltration *via* IFN-I signaling, while simultaneously inducing $CD8^+$ T cell exhaustion. Additionally, *sB.t* synergizes with Apatinib by suppressing VEGFA expression and potentiating anti-angiogenic effects. These dual mechanisms underpin the enhanced therapeutic efficacy observed in the presence of *B.t*.

3.3. B.t regulates VEGFA and IFN-is expression via formic acid secretion

Next, we investigated the mechanism by which *sB.t* regulates *VEGFA* and *IFN-Is* (*IFNA2* and *IFNB1*) expression. Considering that bacterial metabolites are critical mediators of host regulation, we hypothesized that *sB.t* secretes metabolites to exert these effects[36]. Using a 3 kDa molecular weight cutoff filter, we found that the filtered supernatant of *sB.t* retained its ability to inhibit *VEGFA* expression and upregulate *IFN-Is* expression (Fig. 3A and Supporting Information Fig. S4A). Given that most bacterial polysaccharides and toxins exceed 3 kDa, while metabolites are typically smaller than 0.5 kDa, this suggested that small molecular weight metabolites were responsible. We performed gas chromatography-mass spectrometry (GC−MS) analysis to identify these metabolites. Several SCFAs, including formic acid (FA), acetic acid (AA) and butyric acid (BA), were significantly increased in the *sB.t*-co-culture system (Fig. 3B and S4B). Furthermore, in HCC samples from mice treated with vancomycin, FA and BA levels were elevated compared to the PBS group (Fig. S4C).

To evaluate the individual contributions of FA and BA, we tested their effects on *VEGFA* and *IFN-Is* expression in MHCC97-H and Hepa1-6 cells. Sodium formate (SF) significantly inhibited *VEGFA* expression and upregulated *IFN-Is*, whereas sodium butyrate (SB) had no significant effect (Fig. 3C and Fig. S4D). These findings suggest that FA plays a pivotal role in regulating *VEGFA* and *IFN-Is* expression. FA exerts biological effects in mammalian cells by participating in the one-carbon cycle, a metabolic pathway critical for nucleotide biosynthesis and methylation reactions (Fig. 3D). C1-tetrahydrofolate synthase is the key enzyme facilitating SF entry into this cycle, with cytosolic (MTHFD1) and mitochondrial (MTHFD1L) isoforms[9]. By individually knocking down *MTHFD1* and *MTHFD1L*, we observed that the regulatory effects of SF on *VEGFA* and *IFN-Is* were abolished only when *MTHFD1* was knocked down (Fig. 3E, Fig. S4E and S4F). Consistent with this, intracellular levels of key one-carbon cycle products, inosine monophosphate (IMP) and *S*-adenosylmethionine (SAM) were significantly increased after SF treatment or co-culture with *sB.t* (Fig. 3F and G, and Fig. S4G and S4H).

Considering that tumor cells themselves could also produce formic acid, to further clarify the main source of formic acid, we cultured Hepa1-6 cells co-cultured with *sB.t* in media lacking amino acids that played a crucial role in the production of formic acid, including serine glycine, tryptophan, or histidine respectively; and found that intracellular FA concentration significantly decreased after the loss of serine, while slight decreases were observed after the loss of other amino acids (Fig. S4I). After using metronidazole to eliminate intracellular *sB.t*, the intracellular FA levels further decreased, compared to the situation where serine was removed; moreover, in the absence of *sB.t* colonization, this metronidazole treatment did not affect the intracellular FA level (Fig. S4J). To further elucidate this, we transfected siRNA targeting the key gene Serine hydroxymethyltransferase (*Shmt2*), which is involved in serine catabolism to promote FA production, and found that the decrease in intracellular FA levels caused by *sB.t* elimination was much greater than that caused by inhibiting serine catabolism (Fig. S4K and S4L). More importantly, to further verify the correlation between the effects *sB.t* exerted and FA production, we utilized the pSIE1 plasmid system to perform

analysis on the proportion of bacterial specie met criteria ($n = 6$ per group). *P* value by Student's *t*-test, mean ± SEM. (G) Representative fluorescence *in situ* hybridization images of *B.t*-probe detection in the HCC cohort-1 ($n = 26$). *P* value by Student's *t*-test, mean ± SEM. (H) Schematic diagram of the orthotopic mouse model after co-culturing Hepa1-6 cells with *sB.t* for colonization and *in vivo* model. (I) Representative image of Hepa1-6 orthotopic mouse model after indicated treatment. The visible tumor was dissected and weighed. *P* value by one-way ANOVA, mean ± SEM. (J) The *sB.t* load of germ-free HCC model mice was assessed by quantitative polymerase chain reaction ($n = 10$ per group). (K) Relative fold change (compared to Day 15) of luciferase intensity in the HCC somatic mouse model ($n = 6$ per group). *P* value by one-way ANOVA, mean ± SD. (L) The *sB.t* load of germ-free HCC model mice was assessed by quantitative polymerase chain reaction after indicated treatment ($n = 10$ per group). *P* value by one-way ANOVA, mean ± SEM.

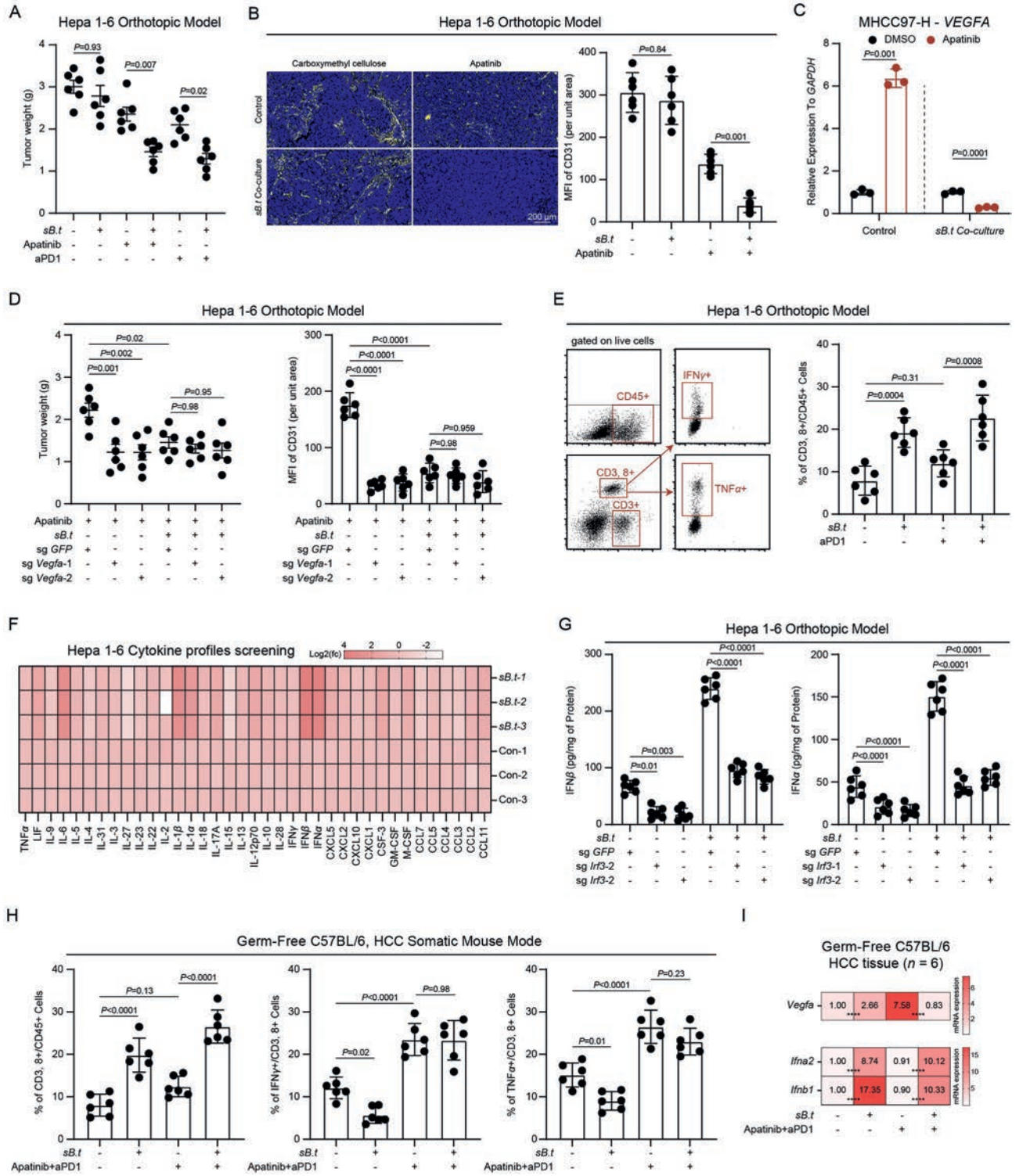

Figure 2 *B.t* promotes the efficacy of Apatinib and aPD-1 by respectively inhibiting VEGFA and promoting IFN-Is transcription (A) Hepa1-6 cells colonized with *sB.t* were used to establish an orthotopic model and subjected to the indicated treatment. The visible tumor was dissected and weighed. *P* value by one-way ANOVA, mean ± SEM. (B) Representative immunofluorescence images of CD31 detection in the Hepa1-6 orthotopic mouse model after indicated treatment ($n = 6$ per group). *P* value by one-way ANOVA, mean ± SEM. (C) Relative *VEGFA* mRNA expression in tumor cells with or without *sB.t* colonization and following Apatinib treatment. *P* value by Student's *t*-test, mean ± SEM. (D) *Vegfa*-knockout Hepa1-6 cells colonized with *sB.t* were used to establish an orthotopic model and subjected to the indicated treatment. The visible tumor was dissected and weighed (left). Immunofluorescence for CD31 MFI is shown (right). *P* value by one-way ANOVA, mean ± SEM. (E) Hepa1-6 cells colonized with *sB.t* were used to establish an orthotopic model and subjected to the indicated treatment. Flow cytometry analysis was used to determine the proportion of intratumoral CD3, 8^+ T cells. *P* value by one-way ANOVA, mean ± SEM. (F) Cytokine

deletion mutations on Formate acetyltransferase or pyruvate formate-lyase (*pflB*) in *sB.t* (Fig. S4M and S4N). After confirming that the formic acid levels in the culture supernatant of Δ*pflB sB.t* were significantly lower than those of *sB.t* (Supporting Information Fig. S5A), we co-cultured the two strains with MHCC97 or Hepa1-6 cells, respectively. We then analyzed the levels of *VEGFA* under Apatinib treatment, as well as the levels of *IFNA2* and *IFNB1* under normal culture. It was also found that in the absence of PflB, the inhibitory effect of *sB.t* on *VEGFA* expression and the promoting effects on *IFNA2/B1* expression were significantly weakened; However, after the addition of exogenous FA, these effects caused by the absence of PflB were significantly reversed (Fig. S5B−S5D). These findings suggest that *sB.t* drives the one-carbon cycle in host cells by producing FA, which regulates *VEGFA* and *IFN-Is* expression. This unveils a novel metabolic interaction between *sB.t* and host cells, mediated by FA, that significantly influences tumor biology and enhances efficacy of therapeutic interventions, particularly the aPD-1 + Apatinib regimen.

To further validate the role of FA *in vivo*, we assessed its impact using the Hepa1-6 based subcutaneous model. Intratumoral injection of SF significantly enhanced the efficacy of the aPD-1 + Apatinib regimen, leading to improved tumor suppression (Fig. 3H). Correspondingly, SF treatment resulted in reduced intratumoral VEGFA levels and elevated IFNα levels (Fig. S5E). Consistent with earlier findings, SF treatment also enhanced $CD8^+$ T cell infiltration within the tumor microenvironment and upregulated the expression of effector molecules, such as IFNγ and TNFα, in these infiltrated T cells (Fig. S5F). More importantly, we inoculated Hepa1-6 cells carrying different *B.t* strains (with normal/deficient formate production) into mice, and found that liver tumors carrying Δ*pflB sB.t* were significantly larger under combinational treatment of aPD-1 antibody and Apatinib compared to those carrying *sB.t* (Fig. S5G). To further investigate the association between FA and *sB.t* in clinical settings, we assembled a second cohort of postoperative hepatocellular carcinoma patients (HCC Cohort-2, $n = 36$). Notably, a positive correlation was observed between intratumoral FA levels and the abundance of *sB.t* (Fig. 3I and Fig. S5H). These findings collectively suggest that *sB.t* enhances the efficacy of the aPD-1+Apatinib regimen in HCC through FA production, thereby establishing a mechanistic link between bacterial metabolism, host immune modulation, and therapeutic response.

3.4. sB.t and FA modulate VEGFA and IFN-is expression via AhR

To investigate the mechanism by which FA regulates *VEGFA* and *IFN-Is* expression, we focused on key transcription factors known to drive HCC progression and influence *VEGFA* transcription and *IFN-Is* suppression. These include Myc proto-oncogene protein (MYC), Signal transducer and activator of transcription 3 (STAT3), Aryl hydrocarbon receptor (AhR), and Hypoxia-inducible factor 1-alpha (HIF-1α), all of which play critical roles in regulating tumor-related gene expression[37−44]. To determine whether FA exerted its effects through these factors, we employed specific inhibitors: EN4 for MYC, C188-9 for STAT3, Ch223191 for AhR, and YC-1 for HIF-1α. Interestingly, we found that FA no longer exerted its regulatory effects on *VEGFA* and *IFN-Is* expression upon inhibition of AhR. However, inhibition of MYC, STAT3, or HIF-1α did not affect the regulatory role of SF on these molecules (Fig. 4A and B, Supporting Information Fig. S6A and S6B). This suggested that the transcription factor AhR was a key mediator of SF's effects on *VEGFA* and *IFN-Is* expression. To further validate the role of AhR, we used additional AhR inhibitors (BAY-218) and generated *AhR* knockout cell lines based on MHCC97-H and Hepa1-6 cells. Both pharmacological inhibition and genetic ablation of AhR led to the loss of SF's regulatory effects on *VEGFA* and *IFN-Is* expression (Fig. 4C−H, Fig. S6C−S6I). In line with this, SF treatment and *sB.t* co-culture resulted in reduced expression of typical AhR target genes, including *CYP1A1*, *CYP1B1*, *TIPARP*, and *AHRR*, in both MHCC97-H and Hepa1-6 cells (Fig. 4I and J, Fig. S6J and S6K). These data provide strong evidence that FA inhibits the transcriptional activity of AhR in HCC cells, suggesting that the FA−AhR pathway plays a critical role in regulating *VEGFA* and *IFN-Is* expression during HCC progression.

To further elucidate the role of AhR in the regulation of VEGFA transcription by FA, we first performed ChIP assays to assess the binding of AhR to the VEGFA promoter. qPCR analysis revealed that SF treatment reduced AhR binding to the promoter region of VEGFA, suggesting that FA interferes with AhR-mediated transcriptional activation of VEGFA (Fig. 4K). Additionally, we constructed luciferase reporters driven by the VEGFA promoter to confirm the functional impact of SF on VEGFA transcription. As expected, overexpression of *AhR* significantly increased the transcriptional levels of *VEGFA* mRNA, as indicated by enhanced luciferase activity (Fig. S6L). However, upon treatment with SF, luciferase signaling was significantly reduced, further supporting the hypothesis that FA inhibits AhR-driven VEGFA transcription (Fig. S6L). AhR is also known to regulate IFN-Is production both transcriptionally and non-transcriptionally. One well-characterized mechanism involves TIPARP, a gene transcribed by AhR, which suppresses IFN-Is production through TBK1. AhR can also inhibit IFN-Is production by directly interacting with STING, leading to its degradation[45]. Our previous data indicated that SF treatment reduced *TIPARP* expression levels, but there were no significant changes in STING levels (Fig. S4M). These findings suggest that SF primarily regulates IFN-Is production through the AhR−TIPARP axis. To further confirm this, we knocked down *TIPARP* in MHCC97-H and Hepa1-6 cells using siRNA transfection. In these cells, the effects of SF on *IFN-Is* expression were largely abolished (Fig. 4L and Fig. S6O), solidifying the role of TIPARP in mediating FA's effects on IFN-Is production. Next, we evaluated the effects of the *sB.t*−FA−AhR axis in *vivo* models. In tumors formed by *Ahr* knockout Hepa1-

detection in cultured supernatants of *sB.t* colonized Hepa1-6 cells after 24 h. Heatmap shows relative fold change of cytokines across independent experiments ($n = 3$). (G) *Irf3*-knockout Hepa1-6 cells colonized with *sB.t* were used to establish an orthotopic model ($n = 6$ per group). ELISA assay was used to determine the intratumoral level of IFNβ and IFNα. *P* value by one-way ANOVA, mean ± SEM. (H) Flow cytometry analysis was used to determine the proportion of intratumoral CD3, 8^+, IFNγ^+/CD3, 8^+, and TNFα^+/CD3, 8^+ T cells. *P* value by one-way ANOVA, mean ± SEM. (I) Relative *Vegfa* and *Ifna2/b1*mRNA expression in germ-free HCC model mice with indicated treatment ($n = 6$ per group). *P* value by one-way ANOVA, mean ± SEM.

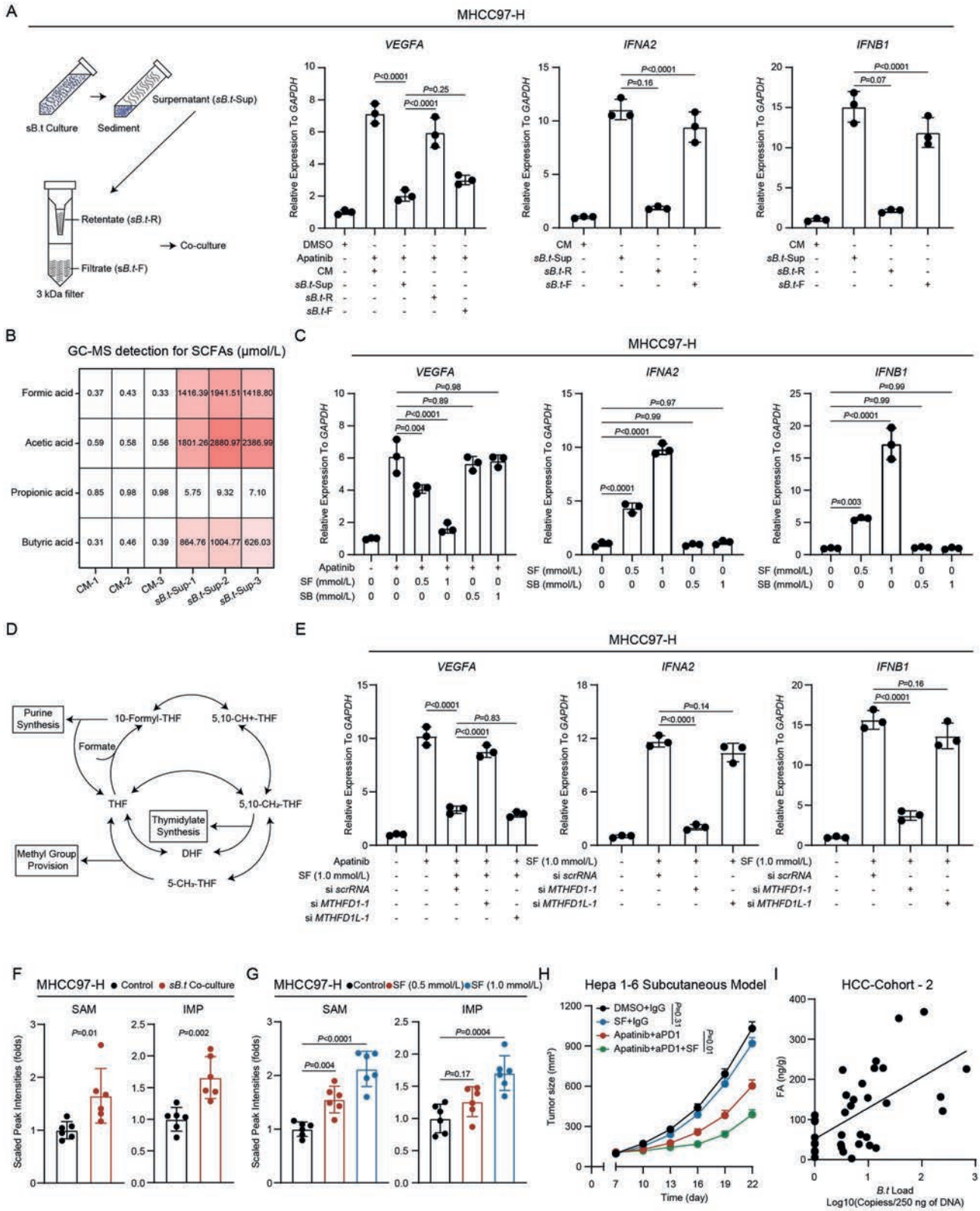

Figure 3 *B.t* regulates VEGFA and IFN-Is expression *via* formic acid (FA) secretion. (A) Relative *VEGFA*, *IFNA2*, and *IFNB1* mRNA expression in MHCC97-H cells following indicated treatment. *P* value by one-way ANOVA, mean ± SEM. (B) Targeted GC−MS metabolite detection in cultured supernatants after 1×10^8 *sB.t* cultured in specifically prepared medium under 12 h was used to measure primary SCFA levels compared to control medium without *sB.t* culture. Heatmap shows relative fold change of extracellular metabolites (rows) across independent experiments ($n = 3$). (C) Relative *VEGFA*, *IFNA2*, and *IFNB1* mRNA expression in MHCC97-H cells following indicated treatment. *P* value by one-way ANOVA, mean ± SEM. (D) Diagram of the primary metabolism pathway of formic acid. (E) Relative mRNA expression levels

6 cells, the presence of *sB.t* no longer enhanced the therapeutic efficacy of the aPD-1 + Apatinib regimen (Fig. 4M). To further clarify the effects of AhR signaling, we constructed mice with liver-specific knockout of *Ahr* (Fig. S6P and S6Q). The transgenic mice were subjected to the somatic HCC model construction and treated with ABX, followed by gavaging *sB.t*. After confirming the colonization of *sB.t* in the liver tumor (Supporting Information Fig. S7A), the mice underwent intraperitoneal injection of tamoxifen. Five days after the tamoxifen injection, the mice were treated with Apatinib and PD-1(Fig. S7B). Consistent with previous results, the combination therapy of Apatinib and aPD-1 antibody achieved better therapeutic effects in the presence of *sB.t* in liver tumors; on the other hand, it was confirmed that knocking out of AhR had already led to a significant reduction in tumor volumes under Apatinib and aPD-1 antibody, while the presence of *sB.t* did not further cause tumor shrinkage (Fig. S7C). The above data suggested that the therapeutic impact of *sB.t* was dependent on AhR. A recent study indicated that gut microbiota dysbiosis can promote HCC progression through the tryptophan−AhR−SREBP2 axis[46]. Here, we found *sB.t* exerted its effect by inhibiting AhR through the secretion of formic acid. Consistent with the study, both co-culture with s*B.t* and formic acid treatment led to downregulation of SREBP2 in Hepa1-6 and MHCC97 cell lines (Fig. S7D and S7E). However, after constructing the *Srebf2* knockout cell line of Hepa1-6 and conducting orthotopic liver inoculation and treatment (Fig. S7F), we found that the absence of *Srebf2* did not affect the sensitizing effect of *B.t* co-culture or FA treatment on the Apatinib + aPD-1 antibody regimen (Fig. S7G and S7H). This result indicated that the initiation stage of a tumor and the post-formation stage of the tumor are two distinct phases; the criticality of the same gene may vary; even the same gene may simultaneously exert completely opposite effects on the tumor's fate in different stages.

Additionally, to assess the therapeutic potential of targeting AhR, we administered the AhR inhibitor CH223191 in combination with the aPD-1 + Apatinib regimen. This combination treatment resulted in significantly smaller tumor volumes compared to the original aPD-1 + Apatinib regimen (Fig. 4N). In line with this, the addition of the AhR inhibitor also led to further suppression of intratumoral VEGFA levels, upregulation of intratumoral IFN-Is levels, and improved functional status of $CD8^+$ T cells (Fig. 4O and Fig. S7I). These results suggest that targeting the *sB.t*−FA−AhR axis can potentiate the efficacy of aPD-1 + Apatinib therapy in HCC by inhibiting VEGFA production, promoting IFN-Is signaling, and enhancing immune response, providing a potential therapeutic strategy for improving treatment outcomes in HCC.

3.5. sB.t and FA repress AhR transcription on downstream genes by inhibiting KPNA2-dependent nuclear translocation

To further investigate the mechanism by which FA inhibits AhR and its downstream transcription, we began by examining the expression levels of AhR in both MHCC97-H and Hepa1-6 cells. We found no significant changes in AhR expression following SF treatment, suggesting that FA does not directly regulate the expression of AhR itself (Supporting Information Fig. S8A). AhR is a ligand-dependent transcription factor, which requires binding to small molecules to undergo nuclear translocation and initiate transcription of downstream genes. Therefore, we next examined the nuclear localization of AhR under different conditions. We observed that the nuclear translocation of AhR was reduced both when cells were co-cultured with *sB.t* and when treated with SF (Fig. S8B and S8C). This indicates that FA and *sB.t* influence AhR's ability to translocate to the nucleus, which is essential for its transcriptional activity. It is known that endogenous ligands such as tryptophan metabolites (Kynurenic acid, KYNA), arachidonic acid metabolites (*e.g.*, lipoxin A4, Prostaglandin PGG2), and heme metabolites (*e.g.*, Bilirubin, Biliverdin) activate AhR in hepatocellular carcinoma cells. Specifically, tryptophan metabolites, such as kynurenine (KYN) and KYNA, are critical for driving the nuclear translocation of AhR due to the high expression of tryptophan 2,3-dioxygenase (TDO2) in HCC[47]. Consistent with this, we found that SF treatment and *sB.t* co-culture suppressed KYN or KYNA-dependent nuclear translocation of AhR (Fig. 5A and B, Fig. S8D and S8E), leading to the downregulation of AhR-mediated transcription of its downstream target genes (Fig. 5C and D, Fig. S8F and S8G). To rule out the possibility that changes in AhR nuclear localization were due to nuclear protein export mechanisms, we used Leptomycin B (LMB), an inhibitor of CRM1, the key protein involved in nuclear export. The results showed that, even in the presence of LMB, the changes in AhR nuclear translocation induced by FA treatment or *sB.t* co-culture remained unchanged (Fig. 5E and Fig. S8H). This suggests that the reduction in AhR nuclear localization is not due to altered nuclear export, but rather a direct effect on the nuclear import of AhR.

Taken together, these data demonstrate that *sB.t* and FA regulate AhR nuclear translocation by modulating its ligand-binding activity, specifically by inhibiting tryptophan metabolite-driven nuclear import[48,49]. This disruption of AhR's nuclear translocation prevents the activation of its downstream gene transcription, which is crucial for regulating both VEGFA and IFN-Is production. Importin-β plays a key role in mediating AhR's nuclear translocation. When we used importazole, an inhibitor of importin-β, we observed that FA no longer influenced AhR translocation under basal conditions or after the addition of KYN (Fig. 5F and G, Fig. S8I and S8J). Importin is composed of importin-α and importin-β subunits, with importin-α acting as an adaptor that selects proteins with nuclear localization sequences (NLS) for nuclear import. Although there are multiple importin-α family (KPNA1-7) members, the specific isoform regulating AhR translocation was unclear. To address this, we conducted a siRNA-based screen and identified KPNA2 as a critical factor. Knockdown of *KPNA2* resulted in a significant reduction in AhR target gene transcription under KYN treatment (Fig. 5H and Fig. S8K). Similarly, the KYN-driven nuclear entry of AhR was substantially impaired when *KPNA2* was knocked down (Fig. 5I and Fig. S8L).

of *VEGFA*, *IFNA2*, and *IFNB1* in *MTFHD1* or *MTFHD1L*-knockdown MHCC97-H cells following indicated treatments. *P* value by one-way ANOVA, mean ± SEM. (F) Relative fold change of SAM or IMP level detected by LC−MS in MHCC97-H cells with *sB.t* colonization. *P* value by Student's *t*-test, mean ± SEM. (G) Relative fold change of SAM or IMP level detected by LC−MS in MHCC97-H cells following SF treatment. (H) Subcutaneously Hepa1-6 bearing mice were constructed and following indicated treatments ($n = 6$ per group). Tumor growth curves were monitored. *P* value by one-way ANOVA, mean ± SEM. (I) The correlation between *B.t* load and concentration of FA in HCC Cohort-2 ($n = 36$).

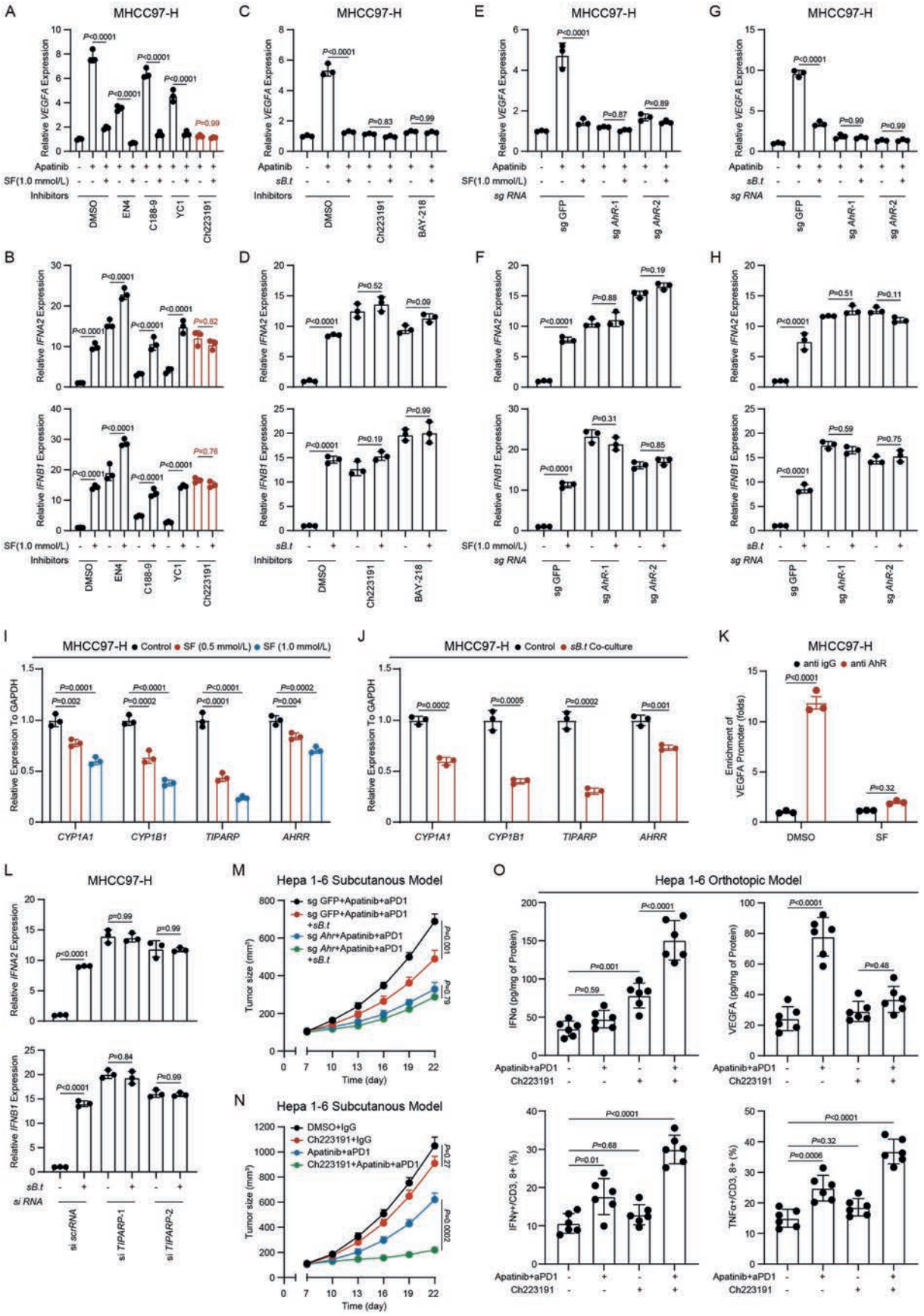
A
MHCC97-H
Relative VEGFA Expression
Apatinib
SF(1.0 mmol/L)
Inhibitors
DMSO
EN4
C188-9
YC1
Ch223191
C
MHCC97-H
Relative VEGFA Expression
sB.t
DMSO
Ch223191
BAY-218
E
MHCC97-H
Relative VEGFA Expression
sg RNA
sg GFP
sg AhR-1
sg AhR-2
G
MHCC97-H
Relative VEGFA Expression
B
Relative IFNA2 Expression
Relative IFNB1 Expression
D
Relative IFNA2 Expression
Relative IFNB1 Expression
F
Relative IFNA2 Expression
Relative IFNB1 Expression
H
Relative IFNA2 Expression
Relative IFNB1 Expression
I
MHCC97-H Control SF (0.5 mmol/L) SF (1.0 mmol/L)
Relative Expression To GAPDH
CYP1A1
CYP1B1
TIPARP
AHRR
J
MHCC97-H Control sB.t Co-culture
Relative Expression To GAPDH
CYP1A1
CYP1B1
TIPARP
AHRR
K
MHCC97-H
anti igG
anti AhR
Enrichment of VEGFA Promoter (folds)
DMSO
SF
L
MHCC97-H
Relative IFNA2 Expression
Relative IFNB1 Expression
sB.t
si RNA
si scrRNA
si TIPARP-1
si TIPARP-2
M
Hepa 1-6 Subcutanous Model
sg GFP+Apatinib+aPD1
sg GFP+Apatinib+aPD1 +sB.t
sg Ahr+Apatinib+aPD1
sg Ahr+Apatinib+aPD1 +sB.t
Tumor size (mm³)
Time (day)
N
Hepa 1-6 Subcutanous Model
DMSO+IgG
Ch223191+IgG
Apatinib+aPD1
Ch223191+Apatinib+aPD1
Tumor size (mm³)
Time (day)
O
Hepa 1-6 Orthotopic Model
IFNα (pg/mg of Protein)
VEGFA (pg/mg of Protein)
IFNγ+/CD3, 8+ (%)
TNFα+/CD3, 8+ (%)
Apatinib+aPD1
Ch223191

To further investigate the direct interaction between AhR and KPNA2, we overexpressed *KPNA2* and performed immunoprecipitation. We found that AhR directly binds to KPNA2, and this binding was enhanced with KYN treatment (Fig. 5J). However, SF treatment or co-culture with *sB.t* resulted in reduced interaction between AhR and KPNA2 (Fig. 5K). These findings suggest that *sB.t* and SF limit AhR function by inhibiting its binding to KPNA2. More compellingly, the armadillo (ARM) domain of KPNA2 is essential for mediating its interaction with the nuclear localization sequence (NLS). We confirmed this by showing that a mutant KPNA2 lacking the ARM domain could no longer interact with AhR (Fig. 5L). Moreover, when we overexpressed either wild-type KPNA2 (WT-KPNA2) or the ARM domain-deleted mutant (ΔARM-KPNA2) in *KPNA2*-knockout MHCC97-H cells (Fig. S8M), we found that only in cells expressing WT-KPNA2 did SF treatment or co-culture with *sB.t* result in reduced AhR nuclear translocation. In contrast, in cells expressing the ΔARM-KPNA2 mutant, neither treatment had any effect on AhR (Fig. 5M and Fig. S8N). These results collectively suggest that *sB.t* and FA modulate AhR nuclear translocation by inhibiting its interaction with KPNA2, specifically through interference with the ARM domain of KPNA2.

3.6. FA facilitates methylation at NLS of AhR leading to diminished binding with KPNA2

We then investigated the detailed mechanism by which *sB.t* and FA regulate the interaction between AhR and KPNA2. Previously, we found that FA derived from *sB.t* could enter the one-carbon cycle. Additionally, we observed that FA enhances purine synthesis and methyl transfer metabolism, both of which are linked to the one-carbon cycle. To probe this further, we used siRNA to knock down Trifunctional purine biosynthetic protein adenosine-3 (*GART*) and *S*-adenosylmethionine synthase isoform type-2 (*MAT2A*), key enzymes involved in purine synthesis and the methyl transfer pathway, respectively[9]. We found that knocking down *MAT2A* blocked the inhibitory effect of SF on the expression of *TIPARP*, whereas knockdown of *GART* had no significant impact (Fig. 6A, Supporting Information Fig. S9A and S9B). To validate this, we employed AGI-24512, a MAT2A inhibitor, and observed that pharmacological inhibition of MAT2A produced similar results to genetic knockdown, restoring the expression of *TIPARP* (Fig. 6B). Furthermore, the expression of *TIPARP* was significantly rescued in cells co-cultured with *sB.t* after *MAT2A* knockout (Fig. 6C and Fig. S9C). Consistently, *MAT2A* knockout also prevented the downregulation of *VEGFA* and the upregulation of *IFNA2* induced by *sB.t* (Fig. 6D and Fig. S9D). These findings suggest that FA exerts its effect on AhR through methyl transfer pathways.

To investigate the role of AhR methylation modifications, we used adenosine dialdehyde (AdOx), a pan-inhibitor of arginine methyltransferases[50], and found that the FA-dependent downregulation of *TIPARP* was abolished under this condition (Fig. 6E). Consistently, AdOx treatment also blocked the effects of SF and *sB.t* on the downregulation of *VEGFA* expression and the upregulation of *IFNA2* levels (Fig. 6E and Fig. S9E). Furthermore, we observed that AdOx reversed the reduction in AhR binding to KPNA2 induced by SF or *sB.t* (Fig. 6F and Fig. S9F), and it promoted AhR nuclear translocation (Fig. 6G and H). These data suggest that arginine methylation on AhR is critical for the action of *sB.t* or FA. More compellingly, we found that SF or *sB.t* treatment increased the levels of arginine mono-methylation and symmetric methylation on AhR (Fig. 6I and Fig. S9G). AhR contains two spaced NLS regions (13−16 and 37−42 aa)[48], both of which are rich in arginine and conserved across multiple species (Fig. S9H). We hypothesized that FA promoted the methylation of arginine in the NLS, blocking its interaction with KPNA2. To test this, we constructed multiple single amino acid mutants, including R13/15/16 K and R38/40/42 K. Interestingly, we found that the R13/15 K mutants showed decreased methylation levels of AhR, whereas the R16/38/40/42 K mutants exhibited no significant changes (Fig. 6J). More importantly, when we constructed a two-site mutant (R13K + R15K), SF treatment or *sB.t*-colonization no longer increased the methylation levels of AhR (Fig. 6K and Fig. S9I). In agreement with this, the methylation level of the R13K + R15K double mutant could not be further decreased under AdOx treatment (Fig. 6L).

4. Discussion

Here, based on the murine HCC somatic model and patient samples, we found that *B.t* significantly contributed to the efficacy of angiogenesis inhibitors combined with ICIs which was the mainstream neoadjuvant treatment regimen in HCC. By secreting formic acid, *B.t* inhibited the expression of VEGFA on the one hand, and promoted the production of IFN-Is upon treatment on the other, thereby further blocking adverse vascularization, and simultaneously creating a hotter immune microenvironment with increased

Figure 4 *B.t* and FA modulate VEGFA and IFN-Is expression *via* AhR. (A, B) Relative *VEGFA*, *IFNA2*, and *IFNB1* mRNA expression in MHCC97-H cells following indicated treatment. *P* value by one-way ANOVA, mean ± SEM. (C, D) Relative *VEGFA*, *IFNA2*, and *IFNB1* mRNA expression in MHCC97-H cells following indicated AhR inhibitor treatment. *P* value by one-way ANOVA, mean ± SEM. (E, F) Relative *VEGFA*, *IFNA2*, and *IFNB1* mRNA expression in *AhR*-knockout MHCC97-H cells following indicated treatment. *P* value by one-way ANOVA, mean ± SEM. (G, H) Relative *VEGFA*, *IFNA2*, and *IFNB1* mRNA expression in *AhR*-knockout MHCC97-H cells with *sB.t* colonization and following indicated treatment. *P* value by one-way ANOVA, mean ± SEM. (I) Relative *CYP1A1*, *CYP1B1*, *TIPARP*, and *AHRR* mRNA expression in MHCC97-H cells following SF treatment. *P* value by one-way ANOVA, mean ± SEM. (J) Relative C *CYP1A1*, *CYP1B1*, *TIPARP*, and *AHRR* mRNA expression in MHCC97-H cells with *sB.t* colonization. *P* value by Student's *t*-test, mean ± SEM. (K) Relative enrichment of AhR to the promoters of VEGFA in MHCC97-H cells was analyzed by ChIP assay. *P* value by Student's *t*-test, mean ± SEM. (L) Relative mRNA expression levels of *IFNA2* and *IFNB1* in *TIPARP*-knockdown MHCC97-H cells with *sB.t* colonization. *P* value by one-way ANOVA, mean ± SEM. (M) Subcutaneously *Ahr*-knockout Hepa1-6 bearing mice were constructed and following indicated treatments ($n = 6$ per group). Tumor growth curves were monitored. *P* value by one-way ANOVA, mean ± SEM. (N, O) Subcutaneously Hepa1-6 bearing mice were constructed and following indicated treatments ($n = 6$ per group). Tumor growth curves were monitored (N). ELISA assay was used to determine the intratumoral level of VEGFA and IFNα (O); Flow cytometry analysis was used to determine the proportion of intratumoral IFNγ^+/CD3, 8^+, and TNFα^+/CD3, 8^+ T cells (O). *P* value by one-way ANOVA, mean ± SEM.

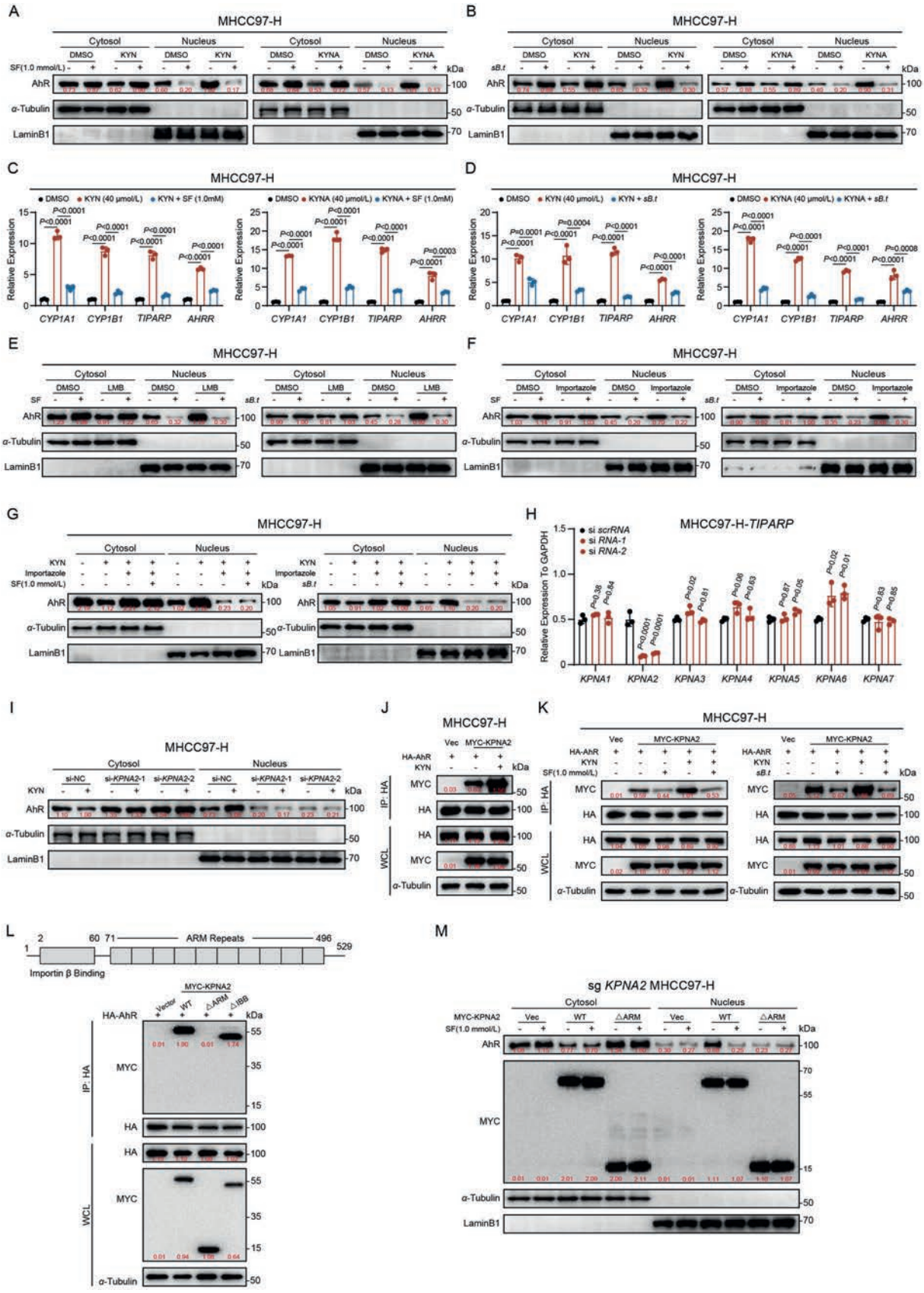

Figure 5 *B.t* and FA repress AhR transcription on 52 downstream genes by inhibiting KPNA2-dependent nuclear translocation. (A) AhR level in cytosol or nucleus of MHCC97-H cells following indicated treatments was validated by Western blot. (B) AhR level in cytosol or nucleus of MHCC97-H cells with *sB.t* colonization and following indicated treatments were validate3d by Western blot. (C) Relative *CYP1A1*, *CYP1B1*,

T-cell infiltration and better functional status which was more conducive to the effect of aPD-1. Mechanistically, through screening, we identified that AhR could directly upregulate VEGFA and inhibit the production of IFN-Is through another target gene, TIPARP. On the other hand, formic acid promoted methylation of residues R13 and R15 on AhR by enhancing methyl transfer metabolism, thus leading to impaired binding between AhR and the nuclear importation adaptor KPNA2; this change further blocked AhR entry into the nucleus during ligand activation and prevented efficient transcription of downstream genes, including VEGFA and TIPARP. From a therapeutic point of view, our findings, on the one hand, suggested that the bacteria and bacterial-associated metabolites in HCC possessed the potential not only as bio-markers to predict therapeutic efficacy, but also as synergistic therapeutics. On the other hand, more importantly, the importance of AhR as a target for HCC was further highlighted as well.

Recent studies have revealed that in addition to host cells, intratumoral bacteria are also an important part of the tumor microenvironment; not only driving tumorigenesis and development, but also influencing the efficacy of multiple treatments and thus are important targets[51−53]. However, current treatment for modulating intratumoral bacteria is extremely limited and non-specific. Specifically, the existing methods of targeting bacteria are primarily dependent upon antibiotics, while nearly all antibiotics that exist can exert effects on multiple species. In this regard, although in our study we found that vancomycin was able to increase the efficacy of Apatinib and aPD-1 combination therapy against HCC and determined that *B.t* played an important role. Whether other gram-negative bacteria also have a significant effect remains worthy of further investigation. On the other hand, although *B.t* was present in tumor mass of HCC patients and correlated with better efficacy of Apatinib combined with aPD-1 therapy, macroscopically, the bacterial composition in humans is quite different from that of mice, and further clarification is needed as to whether the use of vancomycin in humans also alters the level of *B.t* and promotes the associated therapeutic efficacy. A final point to mention is that, at present, there are still relatively few tumor treatment regimens that include using bacteria directly, the most successful case being *Bacillus* Calmette-Guérin (BCG) infusion used in bladder cancer[54]. The key mechanism by which BCG produces good efficacy is the activation of anti-tumor immunity[55]. In our study, *B.t* also showed an important activating effect on anti-tumor immunity. For the interaction of bacteria with the mammalian immune system, current studies have focused on the interaction of immune cells, especially with macrophages. This effect is usually manifested by a vigorous innate immune response, as evidenced by the release of pro-inflammatory factors (IL1β, IL6, etc.) and cell death[56,57]. In the case of tumors, especially when bacteria reside in tumor cells and phagocytosis by macrophages is inhibited. Usually, the effect of molecules that recognize PAMPs is not as clear and robust in tumor cells as it is in immune cells[58,59]. Therefore, for the further development of therapies using bacteria in tumors, it is necessary to further delineate the patterns and effects of interactions with bacteria occurring in tumor cells. In this study, *B.t* was found to be able to colonize hepatocellular carcinoma cells without causing either cell death or significantly affecting proliferation. Although as a gram-negative bacterium, *B.t* releases lipopolysaccharides, which directly leads to pyroptosis in macrophages[60]. However, the levels of the executive molecule of pyroptosis, gasdermin-D, are usually lowly expressed in tumor cells, including the HCC cell lines used here[61]. It may also be that this characterization of tumor cells escaping bacterial-mediated death lays the foundation for transforming an acute inflammatory response into chronic inflammatory remodeling.

Knowledge of bacteria−tumor interactions comes from studies related to intestinal bacteria. To summarize, bacteria usually exert their effects through the expression of their own proteins within the cell or the release of metabolites. In the present study, we found that *B.t* exerted its effect through formic acid. In fact, formic acid is not a metabolite unique to bacteria; formic acid can also be produced in small amounts by mammalian cells[9,16]. In this work, we found that the large amount of formic acid produced by *B.t* promoted methyl transfer metabolism, facilitated methylation of residues R13 and R15 on the AhR, and led to blocked nuclear entry of the AhR and decreased transcriptional function. In previous studies, AhR has been confirmed as a sensor for bacterial tryptophan metabolites such as indole-3-aldehyde or 5-hydroxyindole-3-acetic acid derived from strains like *Lactobacillus reuteri* or *Alistipes onderdonk*[7,62,63]. Typically, AhR is also thought to be activated by direct binding to metabolites[64,65]. However, here, we found that formic acid did not act as a ligand. More interestingly, a recent study found that *Fusobacterium nucleatum* derived formic acid could promote colon cancer progression by activating the AhR in a ligand-like manner. However, this study lacked evidence accounting for direct binding of AhR with formic acid derived from techniques of chemical biology[16]. More importantly, the baseline levels of activation and modification of AhR in tumor cells originating from different tissues vary considerably, and consequently lead to even opposite changes in the signature genes of AhR in different cells, even in the treatment with the same compound[65]. This is also an important reason why AhR exhibits the paradoxical property of promoting or inhibiting tumor progression in different tumors[47].

5. Conclusions

In summary, we uncover a novel bacteria−host interaction mechanism wherein *B.t*-derived formic acid remodels AhR function *via* methylation, establishing this commensal bacterium as both a predictive biomarker and a synergistic therapeutic target for

TIPARP, and *AHRR* mRNA expression in MHCC97-H cells following indicated treatments. *P* value by one-way ANOVA, mean ± SEM. (D) Relative *CYP1A1*, *CYP1B1*, *TIPARP*, and *AHRR* mRNA expression in MHCC97-H cells with *sB.t* colonization and following indicated treatments. *P* value by one-way ANOVA, mean ± SEM. (E−G) AhR level in cytosol or nucleus of MHCC97-H cells following indicated treatments was validated by Western blot. (H) Relative *TIPARP* mRNA expression in MHCC97-H cells after knocking down indicated genes. (I) AhR level in cytosol or nucleus of MHCC97-H cells after knocking down *KPNA2* and following KYN treatment was validated by Western blot. (J) Co-IP and Western blot of HA-AhR and MYC-KPNA2 binding capacity in MHCC97-H cells following KYN treatment. (K) Co-IP and Western blot of HA-AhR and MYC-KPNA2 binding capacity in MHCC97-H cells following indicated treatments. (L) Co-IP and Western blot of HA-AhR and MYC-KPNA2 truncated mutants binding capacity in MHCC97-H cells. (M) AhR levels in cytosol or nucleus of *KPNA2*-knockout MHCC97-H cells after being transfected with indicated MYC-KPNA2 truncated mutants were validated by Western blot.

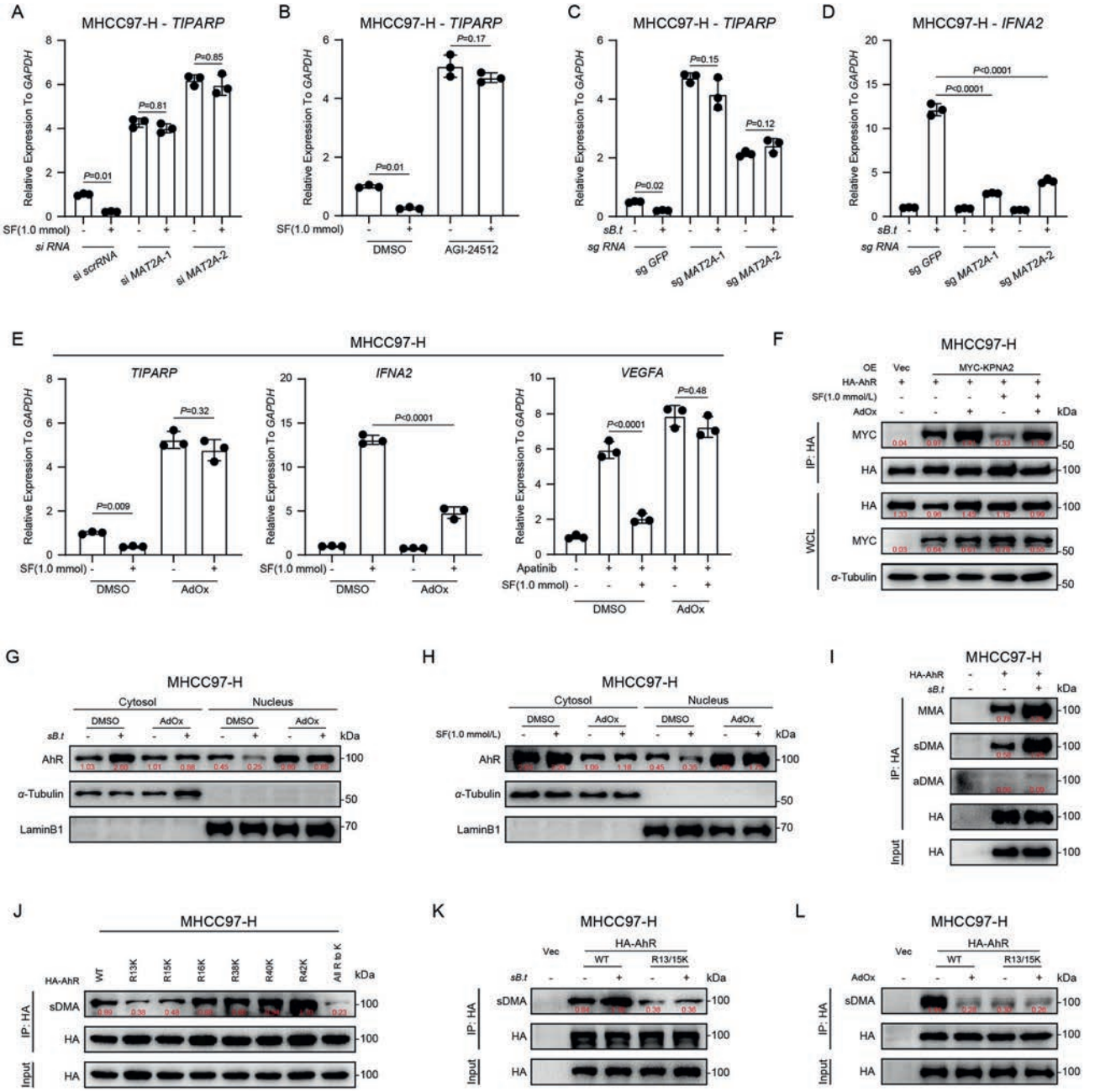

Figure 6 FA facilitates methylation at NLS of AhR leading to diminished binding with KPNA2. (A) Relative *TIPARP* mRNA expression in *MAT2A*-knockdown MHCC97-H cells following SF treatment. *P* value by one-way ANOVA, mean ± SEM. (B) Relative *TIPARP* mRNA expression in MHCC97-H cells following indicated treatment. *P* value by one-way ANOVA, mean ± SEM. (C, D) Relative *TIPARP* and *IFNA2* mRNA expression in *MAT2A*-knockout MHCC97-H cells with *sB.t* colonization and following indicated treatment. *P* value by one-way ANOVA, mean ± SEM. (E) Relative *TIPARP*, *IFNA2*, and *VEGFA* mRNA expression in MHCC97-H cells following indicated treatment. *P* value by one-way ANOVA, mean ± SEM. (F) Co-IP and Western blot of HA-AhR and MYC-KPNA2 binding capacity in MHCC97-H cells following indicated treatment. (G) AhR levels in cytosol or nucleus of MHCC97-H cells with *sB.t* colonization and following indicated treatment were validated by Western blot. (H) AhR levels in cytosol or nucleus of MHCC97-H cells following indicated treatment were validated by Western blot. (I) IP and Western blot of HA-AhR methylation in MHCC97-H cells. (J) IP and Western blot of methylation status of HA-AhR and related mutants at the protein level in MHCC97-H cells. (K) IP and Western blot of methylation status of HA-AhR and related mutants at the protein level in MHCC97-H cells with *sB.t* colonization. (L) IP and Western blot of methylation status of HA-AhR and related mutants at the protein level in MHCC97-H cells following the indicated treatment.

HCC immunotherapy. These findings open new avenues for microbiome-based interventions and underscore the importance of considering intratumoral microbiota in cancer treatment strategies.

Acknowledgments

This study received the funding from Natural Science Foundation of Shanghai Municipal Science and Technology Commission (No. 24ZR1480600, China), National Natural Science Foundation of China (No. 82003910), Henan Clinical Medical Scientist Program (No. HNCMS202406, China), Henan Provincial Medical Science and Technology Project (Nos. SBGJ202402026 and HNSWJW2022029, China), National Key Clinical Discipline Construction Project.

Author contributions

Jiongjiong Lu, Feiling Feng, Chunlei Li, and Ziqing Yu contributed equally to this research. Jiongjiong Lu, Li Luo, Xuemei Guan, Yanxiao Xiang, and Hao Zhuang proposed and designed this study. Jiongjiong Lu, Feiling Feng, Chunlei Li, and Ziqing Yu collected patient samples and conducted experimental research. Jiongjiong Lu, Feiling Feng, Chunlei Li, Ziqing Yu, Tingting Zhang, Anchang Liu, and Qingxiang Gao processed the raw data and conducted the bioinformatic and statistical analysis. Jiongjiong Lu, Feiling Feng, Chunlei Li, Ziqing Yu, Li Luo, and Hao Zhuang made data interpretations. Jiongjiong Lu, Feiling Feng, Chunlei Li, and Ziqing Yu wrote the manuscript draft. Li Luo, Xuemei Guan, Yanxiao Xiang, and Hao Zhuang revised the manuscript. All authors have read and approved the final version of this manuscript to be published.

Conflicts of interest

The authors declare no conflicts of interest.

Appendix A. Supporting information

Supporting information to this article can be found online at https://doi.org/10.1016/j.apsb.2026.06.046.

References

1. Hwang SY, Danpanichkul P, Agopian V, Mehta N, Parikh ND, Abou Alfa GK, et al. Hepatocellular carcinoma: updates on epidemiology, surveillance, diagnosis and treatment. *Clin Mol Hepatol* 2025;**31**: S228−54.
2. Finn RS, Qin S, Ikeda M, Galle PR, Ducreux M, Kim TY, et al. Atezolizumab plus Bevacizumab in unresectable hepatocellular carcinoma. *N Engl J Med* 2020;**382**:1894−905.
3. Ren Z, Xu J, Bai Y, Xu A, Cang S, Du C, et al. Sintilimab plus a bevacizumab biosimilar (IBI305) *versus* sorafenib in unresectable hepatocellular carcinoma (ORIENT-32): a randomised, open-label, phase 2−3 study. *Lancet Oncol* 2021;**22**:977−90.
4. Jiang X, Zhang C, Cao S, Peng Y, Zhao M, Zhang X, et al. Analysis of intertumoural bacteria: opportunities and challenges for cancer therapy. *Acta Pharm Sin B* 2026;**16**:2877−902.
5. Liu B, Zhou Z, Jin Y, Lu J, Feng D, Peng R, et al. Hepatic stellate cell activation and senescence induced by intrahepatic microbiota disturbances drive progression of liver cirrhosis toward hepatocellular carcinoma. *J Immunother Cancer* 2022;**10**:e003069.
6. Yu T, Guo F, Yu Y, Sun T, Ma D, Han J, et al. *Fusobacterium nucleatum* promotes chemoresistance to colorectal cancer by modulating autophagy. *Cell* 2017;**170**:548−63.e16.
7. Zhong S, Sun YQ, Huo JX, Xu WY, Yang YN, Yang JB, et al. The gut microbiota−aromatic hydrocarbon receptor (AhR) axis mediates the anticolitic effect of polyphenol-rich extracts from *Sanghuangporus*. *iMeta* 2024;**3**:e180.
8. Chen L, Zhang K, Liu J, Li X, Liu Y, Ma H, et al. The role of the microbiota-gut-brain axis in methamphetamine-induced neurotoxicity: disruption of microbial composition and short-chain fatty acid metabolism. *Acta Pharm Sin B* 2024;**14**:4832−57.
9. Brosnan ME, Brosnan JT. Formate: the neglected member of one-carbon metabolism. *Annu Rev Nutr* 2016;**36**:369−88.
10. Newman AC, Falcone M, Huerta Uribe A, Zhang T, Athineos D, Pietzke M, et al. Immune-regulated IDO1-dependent tryptophan metabolism is source of one-carbon units for pancreatic cancer and stellate cells. *Mol Cell* 2021;**81**:2290−302.e7.
11. Ma EH, Bantug G, Griss T, Condotta S, Johnson RM, Samborska B, et al. Serine is an essential metabolite for effector T cell expansion. *Cell Metab* 2017;**25**:345−57.
12. Rowe JH, Elia I, Shahid O, Gaudiano EF, Sifnugel NE, Johnson S, et al. Formate supplementation enhances antitumor $CD8^+$ T-cell fitness and efficacy of PD-1 blockade. *Cancer Discov* 2023;**13**: 2566−83.
13. Jin H, Shi Y, Lv Y, Yuan S, Ramirez CFA, Lieftink C, et al. EGFR activation limits the response of liver cancer to lenvatinib. *Nature* 2021;**595**:730−4.
14. Gu CY, Lee TKW. Preclinical mouse models of hepatocellular carcinoma: an overview and update. *Exp Cell Res* 2022;**412**: 113042.
15. Wang X, Cai Z, Wang Q, Wu C, Sun Y, Wang Z, et al. Bacteroides methylmalonyl-CoA mutase produces propionate that promotes intestinal goblet cell differentiation and homeostasis. *Cell Host Microbe* 2024;**32**:63−78.e7.
16. Ternes D, Tsenkova M, Pozdeev VI, Meyers M, Koncina E, Atatri S, et al. The gut microbial metabolite formate exacerbates colorectal cancer progression. *Nat Metab* 2022;**4**:458−75.
17. Porter NT, Larsbrink J. Investigation and alteration of organic acid synthesis pathways in the mammalian gut symbiont *Bacteroides thetaiotaomicron. Microbiol Spectr* 2022;**10**:e0231221.
18. Ryan D, Bornet E, Prezza G, Alampalli SV, Franco de Carvalho T, Felchle H, et al. An expanded transcriptome atlas for *Bacteroides thetaiotaomicron* reveals a small RNA that modulates tetracycline sensitivity. *Nat Microbiol* 2024;**9**:1130−44.
19. Taketani M, Zhang J, Zhang S, Triassi AJ, Huang YJ, Griffith LG, et al. Genetic circuit design automation for the gut resident species *Bacteroides thetaiotaomicron. Nat Biotechnol* 2020;**38**:962−9.
20. Wang Y, Tang Z. A novel long-sustaining system of apatinib for long-term inhibition of the proliferation of hepatocellular carcinoma cells. *OncoTargets Ther* 2018;**11**:8529−41.
21. Yang J, Rui W, Zhong S, Li X, Liu W, Meng L, et al. Symbiotic biofilms formed by *Clostridioides difficile* and *Bacteroides thetaiotaomicron* in the presence of vancomycin. *Gut Microbes* 2024;**16**: 2390133.
22. Qiao H, Tan XR, Li H, Li JY, Chen XZ, Li YQ, et al. Association of intratumoral microbiota with prognosis in patients with nasopharyngeal carcinoma from 2 hospitals in China. *JAMA Oncol* 2022;**8**: 1301−9.
23. Nejman D, Livyatan I, Fuks G, Gavert N, Zwang Y, Geller LT, et al. The human tumor microbiome is composed of tumor type-specific intracellular bacteria. *Science* 2020;**368**:973−80.
24. Fuks G, Elgart M, Amir A, Zeisel A, Turnbaugh PJ, Soen Y, et al. Combining 16S rRNA gene variable regions enables high-resolution microbial community profiling. *Microbiome* 2018;**6**:17.
25. Pham VN, Bruemmer KJ, Toh JDW, Ge EJ, Tenney L, Ward CC, et al. Formaldehyde regulates *S*-adenosylmethionine biosynthesis and one-carbon metabolism. *Science* 2023;**382**:eabp9201.

26. He Y, Zhang Q, Yu X, Zhang S, Guo W. Overview of microbial profiles in human hepatocellular carcinoma and adjacent nontumor tissues. *J Transl Med* 2023;**21**:68.
27. Komiyama S, Yamada T, Takemura N, Kokudo N, Hase K, Kawamura YI. Profiling of tumour-associated microbiota in human hepatocellular carcinoma. *Sci Rep* 2021;**11**:10589.
28. Hugenholtz F, de Vos WM. Mouse models for human intestinal microbiota research: a critical evaluation. *Cell Mol Life Sci* 2018;**75**: 149−60.
29. Leinwand JC, Paul B, Chen R, Xu F, Sierra MA, Paluru MM, et al. IntraHepatic microbes govern liver immunity by programming NKT cells. *J Clin Investig* 2022;**132**:e-17.
30. Nakano V, Piazza RM, Cianciarullo AM, Bueris V, Santos MF, Menezes MA, et al. Adherence and invasion of *Bacteroidales* isolated from the human intestinal tract. *Clin Microbiol Infect* 2008;**14**: 955−63.
31. Liao J, Jin H, Li S, Xu L, Peng Z, Wei G, et al. Apatinib potentiates irradiation effect *via* suppressing PI3K/AKT signaling pathway in hepatocellular carcinoma. *J Exp Clin Cancer Res* 2019;**38**:454.
32. Yang Y, Wang C, Sun H, Jiang Z, Zhang Y, Pan Z. Apatinib prevents natural killer cell dysfunction to enhance the efficacy of anti-PD-1 immunotherapy in hepatocellular carcinoma. *Cancer Gene Ther* 2021;**28**:89−97.
33. Pérez Gutiérrez L, Ferrara N. Biology and therapeutic targeting of vascular endothelial growth factor A. *Nat Rev Mol Cell Biol* 2023;**24**: 816−34.
34. Vesely MD, Zhang T, Chen L. Resistance mechanisms to anti-PD cancer immunotherapy. *Annu Rev Immunol* 2022;**40**:45−74.
35. Snell LM, McGaha TL, Brooks DG. Type I interferon in chronic virus infection and cancer. *Trends Immunol* 2017;**38**:542−57.
36. Fernandes MR, Aggarwal P, Costa RGF, Cole AM, Trinchieri G. Targeting the gut microbiota for cancer therapy. *Nat Rev Cancer* 2022; **22**:703−22.
37. Wei GZ, Martin KA, Xing PY, Agrawal R, Whiley L, Wood TK, et al. Tryptophan-metabolizing gut microbes regulate adult neurogenesis *via* the aryl hydrocarbon receptor. *Proc Natl Acad Sci U S A* 2021;**118**: e2021091118.
38. Yamada T, Horimoto H, Kameyama T, Hayakawa S, Yamato H, Dazai M, et al. Constitutive aryl hydrocarbon receptor signaling constrains type I interferon-mediated antiviral innate defense. *Nat Immunol* 2016;**17**:687−94.
39. Tsartsalis S, Sleven H, Fancy N, Wessely F, Smith AM, Willumsen N, et al. A single nuclear transcriptomic characterisation of mechanisms responsible for impaired angiogenesis and blood−brain barrier function in Alzheimer's disease. *Nat Commun* 2024;**15**:2243.
40. Miar A, Arnaiz E, Bridges E, Beedie S, Cribbs AP, Downes DJ, et al. Hypoxia induces transcriptional and translational downregulation of the type I IFN pathway in multiple cancer cell types. *Cancer Res* 2020;**80**:5245−56.
41. Muthalagu N, Monteverde T, Raffo Iraolagoitia X, Wiesheu R, Whyte D, Hedley A, et al. Repression of the type I interferon pathway underlies MYC- and KRAS-dependent evasion of NK and B cells in pancreatic ductal adenocarcinoma. *Cancer Discov* 2020; **10**:872−87.
42. Sun X, Sui Q, Zhang C, Tian Z, Zhang J. Targeting blockage of STAT3 in hepatocellular carcinoma cells augments NK cell functions *via* reverse hepatocellular carcinoma-induced immune suppression. *Mol Cancer Therapeut* 2013;**12**:2885−96.
43. Lee C, Cheung ST. STAT3: an emerging therapeutic target for hepatocellular carcinoma. *Cancers (Basel)* 2019;**11**:1646.
44. Sequera C, Grattarola M, Holczbauer A, Dono R, Pizzimenti S, Barrera G, et al. MYC and MET cooperatively drive hepatocellular carcinoma with distinct molecular traits and vulnerabilities. *Cell Death Dis* 2022;**13**:994.
45. Ma Z, Li Z, Mao Y, Ye J, Liu Z, Wang Y, et al. AhR diminishes the efficacy of chemotherapy *via* suppressing STING dependent type-I interferon in bladder cancer. *Nat Commun* 2023;**14**:5415.
46. Chen W, Wen L, Bao Y, Tang Z, Zhao J, Zhang X, et al. Gut flora disequilibrium promotes the initiation of liver cancer by modulating tryptophan metabolism and up-regulating SREBP2. *Proc Natl Acad Sci U S A* 2022;**119**:e2203894119.
47. Murray IA, Patterson AD, Perdew GH. Aryl hydrocarbon receptor ligands in cancer: friend and foe. *Nat Rev Cancer* 2014;**14**:801−14.
48. Haidar R, Shabo R, Moeser M, Luch A, Kugler J. The nuclear entry of the aryl hydrocarbon receptor (AHR) relies on the first nuclear localization signal and can be negatively regulated through IMPα/β specific inhibitors. *Sci Rep* 2023;**13**:19668.
49. Murray IA, Reen RK, Leathery N, Ramadoss P, Bonati L, Gonzalez FJ, et al. Evidence that ligand binding is a key determinant of Ah receptor-mediated transcriptional activity. *Arch Biochem Biophys* 2005;**442**:59−71.
50. Yan W, Liu X, Qiu X, Zhang X, Chen J, Xiao K, et al. PRMT5-mediated FUBP1 methylation accelerates prostate cancer progression. *J Clin Investig* 2024;**134**:e175023.
51. Qi Y, Qiu Y, Zhang Y, Zhang L, Xiong H, Yao J. Ferroptosis-based nano-assembly enhanced breast cancer therapy by inhibiting intratumor bacteria. *Acta Pharm Sin B* 2026;**16**:1733−46.
52. Dong W, Li C, Lu J, Weng L, Xu Y, Xu M, et al. Engineered bacteria reprogram tumor microenvironment *via* cell senescence and neutrophil extracellular traps degradation. *Acta Pharm Sin B* 2026;**16**:2332−56.
53. Deng J, Kuang W, Chen W, Zhou E, Wu Y, Yang Z, et al. Intratumoral immune-microbial crosstalk shaped by tumor cell-derived extracellular vesicles encapsulating berberine boosts lung cancer immunotherapy. *Acta Pharm Sin B* 2026;**16**:1090−115.
54. Sanli O, Dobruch J, Knowles MA, Burger M, Alemozaffar M, Nielsen ME, et al. Bladder cancer. *Nat Rev Dis Primers* 2017;**3**:17022.
55. Pettenati C, Ingersoll MA. Mechanisms of BCG immunotherapy and its outlook for bladder cancer. *Nat Rev Urol* 2018;**15**:615−25.
56. Yang Y, Liu J, Liu J, Wei S, Kong X, Mu W, et al. Advances in immune cell-based therapeutic agents for the treatment of inflammation-related diseases. *Cell Mol Life Sci* 2026;**79**:177.
57. Pan LL, Ren ZN, Yang J, Li BB, Huang YW, Song DX, et al. Gut microbiota controls the development of chronic pancreatitis: a critical role of short-chain fatty acids-producing Gram-positive bacteria. *Acta Pharm Sin B* 2023;**13**:4202−16.
58. Takeuchi O, Akira S. Pattern recognition receptors and inflammation. *Cell* 2010;**140**:805−20.
59. Wu J, Chen ZJ. Innate immune sensing and signaling of cytosolic nucleic acids. *Annu Rev Immunol* 2014;**32**:461−88.
60. Vandenabeele P, Bultynck G, Savvides SN. Pore-forming proteins as drivers of membrane permeabilization in cell death pathways. *Nat Rev Mol Cell Biol* 2023;**24**:312−33.
61. Lawlor KE, Murphy JM, Vince JE. Gasdermin and MLKL necrotic cell death effectors: signaling and diseases. *Immunity* 2024;**57**: 429−45.
62. Bender MJ, McPherson AC, Phelps CM, Pandey SP, Laughlin CR, Shapira JH, et al. Dietary tryptophan metabolite released by intratumoral *Lactobacillus reuteri* facilitates immune checkpoint inhibitor treatment. *Cell* 2023;**186**:1846−62.e26.
63. Jing W, Dong S, Xu Y, Liu J, Ren J, Liu X, et al. Gut microbiota-derived tryptophan metabolites regulated by Wuji Wan to attenuate colitis through AhR signaling activation. *Acta Pharm Sin B* 2025;**15**:205−23.
64. Rothhammer V, Quintana FJ. The aryl hydrocarbon receptor: an environmental sensor integrating immune responses in health and disease. *Nat Rev Immunol* 2019;**19**:184−97.
65. Leclerc D, Staats Pires AC, Guillemin GJ, Gilot D. Detrimental activation of AhR pathway in cancer: an overview of therapeutic strategies. *Curr Opin Immunol* 2021;**70**:15−26.